Remote Sensing of Environment 328 (2025) 114871

Contents lists available at ScienceDirect

Remote Sensing of Environment

journal homepage: www.elsevier.com/locate/rse

Thermodynamically constrained retrieval algorithm to estimate subpixel fire properties

Chenchong Zhang [a,*], Yuan Wang [a,*], Jun Wang [b,c], Amber Soja [d], Emily Gargulinski [e,d], David Peterson [f], Olga Kalashnikova [g], Bin Zhao [h,i], Yafang Cheng [j], Fangjun Li [k], Rajan Chakrabarty [l,*]

[a] Department of Earth System Science, Stanford University, Stanford, CA 94305, USA
[b] Department of Chemical and Biochemical Engineering, University of Iowa, Iowa City, IA 52242, USA
[c] Center for Global and Regional Environmental Research, and Iowa Technology Institute, University of Iowa, Iowa City, IA 52242, USA
[d] NASA Langley Research Center, Hampton, VA 23666, USA
[e] National Institute of Aerospace, Hampton, VA 23666, USA
[f] Marine Meteorology Division, US Naval Research Laboratory, Monterey, CA 93943, USA
[g] Jet Propulsion Laboratory, California Institute of Technology, Pasadena, CA 91125-0002, USA
[h] State Key Joint Laboratory of Environmental Simulation and Pollution Control, School of Environment, Tsinghua University, Beijing 100084, China
[i] State Environmental Protection Key Laboratory of Sources and Control of Air Pollution Complex, Beijing 100084, China
[j] Max Planck Institute for Chemistry, Mainz 55128, Germany
[k] Geospatial Sciences Center of Excellence, Department of Geography and Geospatial Sciences, South Dakota State University, Brookings, SD 57007, USA
[l] Department of Energy, Environmental and Chemical Engineering, Washington University in St. Louis, St. Louis, MO 63130-4899, USA

ARTICLE INFO

Keywords:
Fire
Wildfire
Fire radiative power
Fire radiative power flux
Geostationary satellites
Sub-pixel retrieval
Fire area
Combustion conditions
Smoldering
Flaming

ABSTRACT

Satellite-based measurements have been widely used for estimating fire-emitted pollutants based on the parameters of either burned area or fire radiative power (FRP). Fire-related remote sensing additionally requires information on active fire areas and fire temperature at a subpixel scale, as well as the combustion phases (i.e., smoldering and flaming) to infer the plume injection height and to understand the mechanics of resulting atmospheric processes like pyro-convection. The FRP is as a key indicator of fire intensity that is frequently retrieved using infrared signals. The fire properties at a subpixel level, including the effective fire temperature and fire area, can be retrieved by the bi-spectral method. However, these approaches normally neglect the heat transport phenomena and subsequently fail to characterize the fire area that could be composed of different combustion phases (e.g. smoldering, flaming, or a combination of the two). Neglecting the phenomena of heat transfer leads to mis-estimation of the actual fire area and its associated emission profile for combustion products that are a function of the combustion phase. To address this challenge, this work presents a new approach to resolve the effective temperature variation inside each fire pixel using a semi-empirical heat-transfer algorithm. This algorithm utilizes radiance observations from geostationary satellites as inputs. With the aid of fine-spatial-resolution spaceborne and airborne observations, we evaluated and validated the fire retrieval performance on western US wildfires corresponding to the 2019 season. Our results show that FRP obtained through this heat-transfer method exhibits a stronger linear correlation with those retrieved from airborne measurements. Moreover, by analyzing the temperature variation curve obtained using this method, it is possible to further retrieve the fire area under different combustion conditions within the fire pixels.

1. Introduction

Wildfires in the western United States (WUS) have increased in extent, intensity, and frequency over the recent decades (Abatzoglou and Williams, 2016; Westerling, 2016). The fires in the United States have burnt more than 13.7 million acres of land in 2020, while about 65 % of the burned area occurred in the WUS, according to the National Interagency Fire Center (NIFC) report (Zhuang et al., 2021). The

* Corresponding author.
E-mail addresses: chczhang@stanford.edu (C. Zhang), yzwang@stanford.edu (Y. Wang), chakrabarty@wustl.edu (R. Chakrabarty).

https://doi.org/10.1016/j.rse.2025.114871
Received 18 October 2024; Received in revised form 27 April 2025; Accepted 8 June 2025
Available online 21 June 2025
0034-4257/

increased extreme fire events are partly attributed to the elevated atmospheric temperature and aridity (Juang et al., 2022; Wilmot et al., 2022). The changing climate dramatically modulates the availability and flammability of fuels in this region, resulting in more frequent and severe fires (Bradstock, 2010; Krawchuk and Moritz, 2011). Wildfires trigger cascading effects on local ecosystems, and fire emissions pose a greater risk to air quality and human health. A few record-breaking wildfires have been reported in the past few years in the WUS (Brewer and Clements, 2019; Rooney et al., 2020). These large fires not only cause irreversible damage to the local living environment but also affect air quality far downwind through long-range transport of primary pollutants such as carbon monoxide (CO) and black carbon (BC), and the formation of secondary pollutants such as tropospheric ozone (O_3) and secondary organic aerosol (SOA) (Lamsal et al., 2015; Val Martin et al., 2015; Rooney et al., 2020). Understanding the overall role of wildfire in atmospheric chemistry and air quality is a topic of high scientific and public interest.

During the past decade, numerous field campaigns investigated emissions from wildfires, their subsequent transport processes and associated chemical transformation, and their impacts on air quality, regional climate, and human health. Those campaigns include the U.S. Department of Energy's Biomass Burning Observation Project field campaign (BBOP) in the summer of 2013 (Hodshire et al., 2021), Studies of Emissions and Atmospheric Composition, Clouds and Climate Coupling by Regional Surveys (SEAC^{4}RS) from August to September 2013 (Toon et al., 2016), and the joint NOAA/NASA Fire Influence on Regional to Global Environments and Air Quality (FIREX-AQ) in the summer of 2019 (Johnson et al., 2021; Warneke et al., 2023). FIREX-AQ, as one of the most recent field campaigns in the WUS during the fire season, encompassed a variety of measurements onboard multiple observation platforms, including satellites, airplanes, and ground-based mobile laboratories. On the other hand, numerical models of atmospheric chemistry and transport were widely employed to advance understanding of the aggregated impacts of wildfire on air quality and the climate system and to provide valuable information on regulatory and health advisory purposes for decision-making during fire events (Jaffe et al., 2020; Ye et al., 2021).

Accurate estimation of fire emission is a prerequisite to evaluating its environmental impacts in atmospheric models. Different emission inventories can produce factors ranging from two to four in the predicted annual carbon emissions from fires when using the same global climate model (Pan et al., 2020). Aircraft and mobile laboratory measurements provide direct evidence of trace gas and aerosol emission rates. However, the sporadic occurrence and the dynamically evolving nature of wildfires require measurement techniques with broad spatiotemporal coverages and high resolution. Satellite-based products thus have been widely used in estimating emission rates of atmospheric pollutants (Jin et al., 2021; Shi et al., 2019). Two approaches are frequently applied to satellite products to develop fire emission inventories: a burned area (BA) based "bottom-up" approach and a fire radiative power (FRP) based "top-down" approach (Seiler and Crutzen, 1980; Wiggins et al., 2021; Wooster et al., 2005). The widely used bottom-up emission inventories include the Fire INventory from NCAR (FINN) (Wiedinmyer et al., 2011; Wiedinmyer et al., 2023), the Global Fire Emissions Database (GFED) (Giglio et al., 2013; Van Der Werf et al., 2017), and the Fire Locating and Modeling of Burning Emissions (FLAMBE) (Reid et al., 2009). They are built on estimates of a few combustion parameters, such as burned area, fuel types, fuel loads, combustion completeness, and emission factors (Andreae, 2019; Andreae and Merlet, 2001). The bottom-up approach shows advantages in transferring the knowledge from laboratory-determined emission factors, especially for those highly reactive or volatile trace species, into field studies. However, complete statistics on the above-mentioned fire-related parameters often require considerable time, making the bottom-up approach inappropriate for application in near real-time systems.

In contrast to the bottom-up approach, fire emission can be alternatively derived using a top-down approach involving the multiplication of the satellite-derived FRP with the specified smoke emission factors and coefficients (Kaufman et al., 1998; Ichoku and Kaufman, 2005). The Global Fire Assimilation System (GFAS) (Kaiser et al., 2012), the Fire Energetics and Emissions Research (FEER) (Ichoku and Ellison, 2014), and the Quick Fire Emissions Dataset (QFED) (Darmenov and da Silva, 2015) exemplify the top-down inventories. The top-down approach reduces the dependency on the estimates of fuel and combustion metrics required by bottom-up methods (Wooster et al., 2005). Moreover, satellites can sensitively detect excessive radiant energy provided an active fire covers less than 0.1 % of the pixel area (Andela et al., 2015; Whitburn et al., 2015), making this approach more sensitive to small-scale and early-stage fires. The FRP-based approach shows the potential for near real-time retrievals because it bypasses the latency intrinsically associated with the bottom-up inventories (Mota and Wooster, 2018). FRP data are widely retrieved through the products from different satellite platforms. FRP is frequently derived from the conversion of single-waveband radiance at middle-infrared band (∼ 4 μm) (Wooster et al., 2003). This method computes the pixel-based FRP (FRP_{MIR}) through the difference in spectral radiance between the fire pixel and adjacent background (Giglio et al., 2016; Schmidt, 2020). Wildfire intensity characterized by FRP commonly presents a robust diurnal cycle that reaches its peak in the midafternoon (Giglio, 2007; Prins and Menzel, 1992). This temporal-dependent pattern is consistent with the observed fire emission rates (Andela et al., 2015; Li et al., 2019).

Although FRP has been proven helpful in inferring the emission rates of primary pollutants, it alone may still cause significant estimation uncertainties under different combustion scenarios. For example, fire temperature and combustion type are crucial in determining the relative contents of various pollutants in emissions (Rein, 2013; Sofan et al., 2019). Besides, many studies require FRP data and other ancillary information to assess fire impacts on the atmosphere. For example, fire area at the subpixel scale is also needed in the plume-rise models to estimate the convective injection height (Grell and Freitas, 2014; Gonzi et al., 2015). Similar fire parameterizations have been applied to a plume-rise-enabled chemical transport framework to evaluate the model prediction of boundary layer heights (Thapa et al., 2022). In addition to fire area and FRP, fire temperature and meteorology should also be considered to understand the atmospheric perturbation processes (Kahn et al., 2007; Peterson et al., 2014; Peterson et al., 2022).

It is becoming clear that fire metrics at the subpixel level are essential for various research and applications. Driven by the need for better subpixel fire detection and characterization, the US Muon Space and the Canadian Space Agency are planning to launch FireSat and WildFireSat Constellations with an average ground sample distance of 80 m and 200 m correspondingly and various degrees of saturation. NASA is actively contributing to fire technology, investing in the development of airborne and space-borne unsaturated sensors. For example, the compact Fire Infrared Radiance Spectral Tracker (c-FIRST) is a NASA Earth Science Technology Office (ESTO) Instrument Incubator Project (IIP) competitively selected in 2021 (Gunapala et al., 2023a,b). The instrument, currently at Technology Readiness Level (TRL) 4, is designed to meet a critical need for small, lightweight, relatively low-power satellite sensors operating at short-wave infrared to mid-wave infrared wavelengths (1–5 μm) with fine spatial resolution from orbit (∼60 m) and extremely high dynamic range (>100 dB). c-FIRST will demonstrate the measurement of spectral radiance and derivation of associated temperatures from intense landscape fires, volcanoes, and other high-temperature targets, obtaining unsaturated images where current, state-of-the-art satellite detectors saturate and would complement low-spatial but higher temporal resolution observations of fire energetics available from currently operating satellite sensors.

The bi-spectral method has been widely used to retrieve fire size and temperature at a subpixel level (Dozier, 1981). Unlike single-band method mentioned above, the bi-spectral method resolves the subpixel fire size and temperature by using the measurements of radiances at both middle-infrared (MIR) and thermal infrared (TIR) wavebands. The pixel-based FRP (FRP_{BS}) is then computed by the Stefan-Boltzmann relationship given by

$$FRP_{BS} = \sigma\left(T_f^4 - T_b^4\right) p S_{pix}, \tag{1}$$

where σ is the Stefan-Boltzmann constant, T_f and T_b are fire and cool background temperatures, respectively, p is the fraction of the fire area in a certain pixel, and S_{pix} is the area of the fire pixel. The traditional bi-spectral algorithm assumes a fire pixel can be well-separated by two distinct effective temperatures, T_f and T_b, which represent the kinetic temperature of the fire area and cool background, respectively (Peterson et al., 2013; Giglio and Schroeder, 2014). However, this assumption mischaracterizes the cases in which active fire areas are normally a mixture of areas with different combustion phases. Moreover, this method completely neglects the transport of energy fluxes, which results in temperature discontinuities at the edge of the retrieved fire area.

This work aims to introduce a new approach that resolves the sub-pixel fire properties by applying a thermodynamically constrained algorithm to the pixel-based geostationary remote sensing data. This algorithm resolves a function representation of the continuously varying temperature inside a fire pixel. Fire parameters, including fire area, fire temperature, combustion phases, and a pixel-based FRP, can be retrieved based on this temperature function. With the aid of coincident remote sensing and in situ measurements during 2019 FIREX-AQ campaign, we can evaluate the performance of this new algorithm.

2. Data sources and data preprocessing

2.1. GOES-R active fire products

The Geostationary Operational Environmental Satellites-R Series (GOES-R) satellites were designed to generate high-temporal-resolution observations of the Earth's surface and the atmosphere. GOES-16 (GOES-East) and 17 (GOES-West, replaced by GOES-18 in January 2023) are two operational GOES-R series satellites at 75.2° W and 137.3° W now over the equator, respectively. The Advanced Baseline Imager (ABI) aboard GOES satellites is a 16-channel passive imaging radiometer that provides continuous radiance imagery with an effective 0.5–2.0 km resolution at nadir (Schmit et al., 2017). It monitors atmospheric, oceanic, and other environmental conditions in a default mode, producing a full disk image every 10 min, a Continental US (CONUS) image every 5 min, and two regional images every 60 s (Schmit et al., 2017).

The Fire Detection and Characterization (FDC) product is the active fire product derived from ABI. FDC builds upon the heritage of the Wildfire Automated Biomass Burning Algorithm (WFABBA), and it includes a data collection of FRP obtained by single-band MIR approach (Prins et al., 1998; Schmidt and Prins, 2003), along with retrievals of fire temperature and area from a modified Dozier's method. In this study, we mainly utilized the ABI brightness temperatures/radiances at channel 7 (centered at 3.9 μm) and channel 13 (centered at 11.2 μm) and applied a semi-empirical algorithm established based on a thermodynamic theorem to retrieve the temperature variation function inside a fire pixel. This new method is different from the Dozier's method and will be detailed in section 3. Additionally, we calculate the FRP based on the retrieved temperature variation function, which also distinguishes it from the single-band MIR method. The GOES fire pixels used in the following case study almost never reach the bands' saturation temperatures (400 K for 3.9 μm band and 330 K for 11.2 μm band). The new retrievals of FRP were compared to those obtained by the MIR method and further correlates to the retrieved FRP from other observational platforms that have a finer spatial resolution, as introduced in the section 5. FDC products used in this study are archived in FIREX-AQ online data repository (https://www-air.larc.nasa.gov/cgi-bin/ArcView/firexaq).

2.2. VIIRS 375-m active fire products

Active fire products processed from the visible infrared imaging radiometer suite (VIIRS) aboard polar-orbiting satellites are used in this study to assess the retrieved FRP from GOES ABI products at those coincident locations. VIIRS is one of the vital radiance receptors aboard the Suomi National Polar-orbiting Partnership (S-NPP) and NOAA's polar-orbiting joint polar satellite system (JPSS) series of satellites (Schueler et al., 2002; Xiong et al., 2014; Wolfe et al., 2013). It is a 22-channel whiskbroom radiometer ranging from the visible to the thermal infrared bands. The VIIRS instrument is built upon the heritage of MODIS. Both the MODIS and VIIRS instruments share many common features in terms of geometry and retrieval algorithms. Several studies have shown that VIIRS has the potential to replace MODIS as a viable alternative for global burned area mapping (Fernández-Manso and Quintano, 2020; Li et al., 2019; Ouattara et al., 2024). The level-2 VIIRS 375-m active fire product from S-NPP (VNP14IMG) that contains geolocation information and pixel-based FRP of fire spots is used in the study (Csiszar et al., 2014; Schroeder et al., 2014). The fire detection is primarily driven by high-resolution imagery band I4 centered at 3.74 μm with a saturation temperature of 367 K. I4 channel data is complemented by band I5 (centered at 11.45 μm) with a higher saturation temperature of about 380 K. They both have a nominal spatial resolution of 375 m. This detection algorithm was tuned to optimize its response over small fires while balancing the occurrence of false alarms. Due to the radiance at I4 band being prone to saturation when observing intense fires, the FRP values are mainly retrieved by using the MIR method based on the signal of 750-m dual-gain M13 (4.05 μm) band. M13 band is saturated at temperatures of 343 K and 634 K at high and low gain settings, respectively (Csiszar et al., 2014). The retrieved FRP is then equally distributed to the collocated I-band fire pixels to generate the final 375-m active fire product. Low-confidence fires are excluded from the analysis before comparing with the collocated GOES FRP retrievals (Giglio et al., 2003; Csiszar et al., 2014; Schroeder et al., 2014; Li et al., 2018). The VIIRS FRP data used in this study are archived in the NASA Fire Information for Resource Management System (FIRMS).

2.3. FRP and combustion classifications obtained by MASTER

FRP and other associated fire parameters from the airborne platform are used in this study to understand the relationship with those retrieved from geostationary datasets. We use the data from the Moderate Resolution Imaging Spectroradiometer (MODIS)-Advanced Spaceborne Thermal Emission and Reflection Radiometer (ASTER) airborne simulator (MASTER) aboard NASA DC-8 aircraft to study the fire characteristics during the 2019 FIREX-AQ campaign. Retrieval of MASTER FRP is implemented by the conversion of detected radiance at the mid-infrared band (~4 μm) (Wooster et al., 2003; Wooster et al., 2005).

MASTER active fire detection algorithm is based on the contextual algorithm developed for MODIS (Giglio et al., 2003). Retrieval of FRP is provided for every pixel and used to calculate the flaming and smoldering combustion phases of a fire using the MASTER 4 μm spectral band (band 32) (Wooster et al., 2003; Wooster et al., 2005). The band 32 of MASTER instruments saturate at about 483 K. Pixels with 4 μm radiance values greater than 99.5 % of the maximum value are classified as saturated (Giglio et al., 2003; Hook et al., 2021). Combustion classification is another critical metric provided by MASTER. A pixel is classified as being in smoldering combustion if its 4 μm brightness temperature is higher than two standard deviations above the mean value of the non-fire 4 μm background brightness temperature, and meanwhile, the pixel's 11 μm brightness temperature is higher than one standard deviation above the mean background 11 μm brightness temperature. A flaming pixel is defined similarly as its 4 μm brightness temperature exceeds three standard deviations of the 4 μm brightness temperature of background pixels. Its 4 μm brightness temperatures must be at least 100 K higher than the brightness temperatures at the 11 μm band. The information on the combustion phase is also utilized in this study to compare with those derived from the GOES retrievals.

2.4. Data preprocessing for correlation analysis

The subpixel algorithm was applied to the GOES active fire product to retrieve the objective fire parameters. The performance of this subpixel algorithm was assessed through those retrieved parameters of the collocated VIIRS-GOES pixels and MASTER-GOES pixels. Two types of processes were employed in this study to find the matched collocated pixel samples among active fire products. The ray-casting algorithm was applied here to determine whether the centers of the fine-spatial-resolution pixels were inside or outside a coarse-resolution pixel. The pixel-based FRPs of those collocated fine-resolution pixels were aggregated and compared with the FRP of the coarser GOES FRP. This method is based on the geographic location of the pixel center, maximizing the sample size for correlation analysis. In addition to the ray-casting method, we applied the Density-Based Spatial Clustering of Applications with Noise (DBSCAN) method to aggregate the pixel-based FRP into clusters for collocation analysis as well (Ester et al., 1996; Shivanasab et al., 2021). For each cluster, the neighborhood of an assigned distance (quantified by the epsilon value) contains at least a minimum number of fire pixels (Khan et al., 2014). This clustering algorithm does not require a predefined number of clusters, making it effective for handling irregular-shaped fire regions and distinguishing possible noisy pixels. The optimal epsilon is determined by the knee value using k-th nearest neighbor's algorithm and the minimum number of pixels was tuned by considering the relative pixel size of two selected fire products.

Due to the much finer spatial resolution of MASTER pixels than the GOES pixels, those MASTER detected fire pixels can be considered as points or spots. These pixels can always be found within certain GOES fire pixels using the ray-casting algorithm. However, applying the ray-casting algorithm to VIIRS pixels near the GOES pixel boundaries may encounter the mismatch problem. Therefore, we applied the ray-casting algorithm to find the collocated MASTER-GOES pixel pairs. For VIIRS-GOES collocation analysis, we applied both the ray-casting algorithm and the DBSCAN method to compare their pixel-based and cluster-based fire parameters, respectively.

3. An improved algorithm to retrieve subpixel fire properties

3.1. Fire area and temperature retrievals at a subpixel level

FRP is the portion of the energy radiated from the burning fuel. Theoretically, it is computed by actual fire size and temperature according to:

$$FRP_{\mathrm{Theo}} = e_{\mathrm{fire}}\sigma \sum_{k=1}^{N} S_{\mathrm{fire},k} \bullet T_k^4, \tag{2}$$

where e_{fire} is the emissivity of fire, σ is the Stefan-Boltzmann constant which is equal to 5.6704×10^{-8} W • m^{-2} • K^{-4}, $S_{\mathrm{fire},k}$ is the actual area of the k-th subpixel fire region, and T_k is the fire kinetic temperature of the subregion.

Eq. (2) requires the subpixel fire sizes and temperatures in a hotspot pixel to compute the FRP. Moderate-spatial-resolution imaging systems cannot directly detect those fine temperature distributions. Therefore, FRP values are mainly obtained from either the observed MIR radiances of the hotspot pixel or the bi-spectral method, which retrieves the fire size and fire temperature by assuming all N thermal components have the identical kinetic temperature (Dozier, 1981; Wooster et al., 2005; Wooster et al., 2003). The MIR radiance approach is applied in the GOES-R FDC Algorithm and the VIIRS 375-m S-NPP Active Fire Product to estimate pixel-based FRP. This method assumes that FRP per unit surface area is linearly proportional to the spectral radiance recorded in the MIR waveband, which is performed by the following equation:

$$FRP_{\mathrm{MIR}} = \frac{S_{\mathrm{pix}}\sigma e_{\mathrm{fire}}}{a e_{MIR}}\left(L_{MIR} - L_{MIR,b}\right), \tag{3}$$

where S_{pix} is the area of the fire pixel, e_{MIR} is the emissivity of the detected fire pixel at the MIR spectral band. a is an instrumental specific constant determined by the empirical best-fit relationship. It is equal to 3.0×10^{-9} W·m^{-2}·sr^{-1}·μm^{-1}·K^{-4} for GOES-R fire characterization algorithm and 2.88×10^{-9} W·m^{-2}·sr^{-1}·μm^{-1}·K^{-4} for VIIRS sensor-specific active fire algorithm (Wooster et al., 2003; Csiszar et al., 2014; Schmidt and Prins, 2003). L_{MIR} and $L_{MIR,b}$ are radiances of the fire-containing pixel and the non-fire background pixel at the MIR band.

Another approach that was extensively applied to the computation of FRP is the bi-spectral method. This method works well when the target brightness temperature differs significantly from the background temperature at the selected wavelengths. The first step is retrieving the fire area and fire temperature at the subpixel scale. A fire pixel that contains a sub-region of fire with a uniform effective temperature T_{f} and a fire area fraction p emits radiances L_4 and L_{11} in specific MIR and TIR bands, respectively. The following equations give the relationships:

$$L_4 = \tau_4 p B\left(\lambda_4, T_{\mathrm{f}}\right) + (1-p)L_{4,\mathrm{b}} \tag{4}$$

$$L_{11} = \tau_{11} p B\left(\lambda_{11}, T_{\mathrm{f}}\right) + (1-p)L_{11,\mathrm{b}}, \tag{5}$$

where $B(\lambda_{4\text{ or }11}, T_{4\text{ or }11})$ is the spectral radiance of an object with temperature $T_{4\text{ or }11}$ at the wavelength $\lambda_{4\text{ or }11}$ computed by the Planck function. The explicit form of the Planck function used in this study is provided in Eq. S1 and S2. τ_4 and τ_{11} represent the upward atmospheric transmittance at 4 μm and 11 μm, respectively. In this study, p, as stated in Eq. (1), is the fraction of fire area in each fire pixel. The background radiances at the top of the atmosphere (TOA), $L_{4,\mathrm{b}}$ and $L_{11,\mathrm{b}}$, are defined as

$$L_{4,b} = \tau_4\left[e_{4b}\mathrm{B}(\lambda_4, T_{\mathrm{b}}) + (1-e_{4b})L_{4,\mathrm{ref}}\right] \tag{6}$$

$$L_{11,b} = \tau_{11}\left[e_{11b}B(\lambda_{11}, T_{\mathrm{b}}) + (1-e_{11b})L_{11,\mathrm{ref}}\right], \tag{7}$$

where e_{4b} and e_{11b} denote the assumed background surface emissivity at 4 μm and 11 μm, respectively. The reflectivity of the opaque pixel with emissivity e is equal to $(1-e)$. $L_{4\text{ or }11,\mathrm{ref}}$ is the solar radiance reflected by land surface at the λ_i μm band. In the current model setting, the contribution of $L_{4\text{ or }11,\mathrm{ref}}$ to background, was temporarily set to zero. Peterson and Wang (2013) pointed out that the viewing zenith angle and column water vapor content affect the differences between atmospheric-corrected radiances and radiances at surfaces. In this study, the processed data were obtained from geostationary satellite imagers, with relatively fixed viewing angles towards the objective region, and the retrievals were mainly applied to wildfire events occurring in that region with a time window of around one week. Given the spatial and temporal constraints, the variations of the stationary satellite's viewing angles were negligible. The effects from variations in surface emissivity and atmospheric column water vapor are minor at 4 μm brightness temperature. As a result, the background temperature, T_{b}, can be approximated by the brightness temperature of fire-free pixels, T_{4b} (Kaufman et al., 1998; Peterson and Wang, 2013). Fire is generally considered as a black body, so its emissivity can be approximated as one. T_{f} and p are retrieved by combining Eq. (4) to Eq. (7) with reasonable corrections for water vapor attenuation and semi-transparent clouds (Peterson and Wang, 2013; Peterson et al., 2013). The subpixel fire algorithm of GOES FDC is an application of this approach, which utilizes the radiances at ABI Channels 7 (3.9 μm) and 14 (11.2 μm) to quantify T_{f} and p (Schmidt and Prins, 2003; Schroeder et al., 2010; Schroeder et al., 2008). Although GOES FDC product uses a modified Dozier method to retrieve both active fire area and effective fire temperature, it still calculates FRP using the MIR method defined by Eq. (3), rather than the bi-spectral method used in Eq. (1) due to considerations of computational cost and reliance on the accuracy of background temperature measurements.

3.2. Heat transfer phenomena in a fire pixel

3.2.1. Model equations related to the heat transfer process

Algorithms for deriving subpixel fire properties based on satellite products are limited by the amount of wildfire-related input data, resolution, and computational cost considerations. As a result, they often require simplifications of real combustion scenarios to obtain those effective subpixel parameters. The Dozier bi-spectral method assumes that all fires inside one pixel have the same kinetic temperature, while the temperature of the non-fire portion in the same pixel equals the background temperature. However, the realistic wildfire areas are often composed of regions in different stages of combustion, such as smoldering and flaming combustion. They have varied radiant energy transfer efficiencies and emission rates of pollutants to the ambient environment. Transitions between different combustion states are continuously occurring during the spread of fires. The retrieval of a unique effective temperature using the traditional bi-spectral method neglects the diversity of temperature variation and combustion conditions in a detected fire pixel, and it will lead to inaccurate estimates of fire energetics and emissions.

Resolving the detailed temperature variations at any scales of a fire requires considering the heat transfer phenomena among the above-ground ignited biomass, the surrounding atmosphere, and the soil beneath the canopies. In this study, we proposed a simplified model that flattens the abovementioned fire-related mediums into a plane that allows the transport of fire energy and the latent heat released/absorbed by the water phase change. The flattened plane, named soil-biomass plane (SBP), is a term for the mixture of soil solid particles, liquid water contained in soil and vegetation, and air in the soil pores that contains water vapor. The thermal properties of the SBP are determined by the relative abundance of the species in different phases. Resolving the complete heat transfer phenomena requires considering energy conservation law and the equilibrium of water between liquid and gaseous phases. The complete equation that governs the heat flow can be written as Eq. (8):

$$C_s\frac{\partial T}{\partial t} - L_v\rho_w\frac{\partial \omega}{\partial t} - \nabla\bullet(\kappa\nabla T) + \omega\rho_a c_p \nabla\bullet(\overrightarrow{u_v}T) = 0, \tag{8}$$

where C_s is the volumetric heat capacity of the SBP, L_v is the latent heat of vaporization of water, ρ_w is the density of water, and ω is the air-filled porosity of the SBP. The first two terms characterize the temporal exchange of sensible and latent heat attributed to temperature change and water vaporization. Furthermore, κ is the thermal conductivity of SBP, ρ_a is the air density, c_p is the specific heat capacity of air, and $\overrightarrow{u_v}$ is the effective velocity of soil airflow. The positive direction of this vector is defined as the direction away from the center of the fire. The third and fourth terms quantify the heat fluxes by conduction and advection, respectively. Within SBP, heat transfer by radiation is much weaker than that by the advection-diffusion process. Hence, we neglected the radiation term in Eq. (8). Note that obtaining a converging solution to Eq. (8) is computationally expensive. It is not feasible to apply the complete form of the above-mentioned governing equation to each fire pixel. To reduce computational cost, the first assumption we made here was that the heat transfer in each fire pixel always reaches its steady state at the time of observations, and thereby, two time-variant terms were omitted. Secondly, the brightness temperature of a fire pixel was determined by the effective temperature of SBP, while the energy exchange between the SBP and the air above, and heat fluxes along the vertical direction beneath the land surface, were neglected. Finally, the heat flux direction in each fire pixel was regarded as unidirectional. Note here a strict solution to Eq. (8) requires consideration of heat transfer in all directions, especially when the thermal conductivity of the medium is anisotropic. Here we made the abovementioned assumptions are primarily based on lowering the computational cost and avoiding too many undetermined parameters due to the limited observational data. These assumptions degrade the original heat transfer problem to a one-dimensional equation. The simplified equation is written as:

$$\frac{d}{dx}\left(\kappa\frac{dT}{dx}\right) = c_p\rho_a\omega\overrightarrow{u_v}\frac{dT}{dx}, \tag{9}$$

In this equation, the positive x direction was defined as the direction from the fire center to the edge of the pixel. The temperatures at the pixels' edges were used as boundary conditions to solve Eq. (9). The background brightness temperature at 4 μm was used here as an estimate of kinetic background temperature since the column water vapor effects on atmospheric transmittance are minor at that wavelength. Background temperatures at boundaries were set to equal the 4 μm background temperature of the fire pixel. By solving this governing thermal equation, we can calculate an effective temperature variation function.The schematic of the retrieved temperature variation using this heat transfer algorithm is illustrated in Fig. 1c. As a comparison, the retrievals of a homogeneous fire temperature assumption and the temperature variations retrieved by the traditional bi-spectral method are shown in Fig. 1a and b, respectively. Fig. 1c depicts the subpixel fire model coupled with the heat transfer algorithm proposed in this study. The retrieved fire region has a peaking constant fire temperature, with a gradually decreasing value towards pixel edges. Note here that the heat transfer model is more applicable to large-scale wildfires. In the absence of topographic constraints and with sufficient fuel availability, the fire perimeter can extend to its maximum extent across the entire pixel.

3.2.2. Parameterizations of heat transfer equations

To solve Eq. (9), it is necessary to first define the parameters in the equation. Here, we use the thermodynamic parameters of soil to represent the thermodynamic parameters of SBP in Eq. (9). The heat transfer model employs basic assumptions and parameterizations, such as those of De Vries and Van Wijk (1963), with minor simplifications and modifications. Similar processes have been applied by Campbell et al. (1994) and Massman (2012). The bulk conductivity κ in Eq. (9) in the current model was expressed as the weighted sum of the thermal conductivities of soil compositions, including conductivity of solid particles (κ_s), water (κ_w), and wet air (κ_a),

$$\kappa = \frac{f_s\kappa_s + f_w\kappa_w + f_a\kappa_a}{f_s + f_w + f_a}. \tag{10}$$

κ_s is a soil property parameter that is independent of ambient conditions. In this study, the value of κ_s is 2.0 W/(m • K), a typical value for Palouse B type soil. κ_w and κ_a are both temperature-dependent variables that can be written as:

$$\kappa_w = 0.554 + 2.24\times10^{-3}\ T_c - 9.87\times10^{-6}\ T_c^2, \tag{11}$$

$$\kappa_a = 0.024 + 7.73\times10^{-5}\ T_c - 2.6\times10^{-8}\ T_c^2 + \kappa_L, \tag{12}$$

where T_c is the Celsius temperature. Soil air conductivity κ_a is expressed as the sum of dry air conductivity and a vapor term, κ_L, that characterizes the latent heat transfer due to the existence of water vapor. κ_L is computed as:

$$\kappa_L = \frac{H_v h\phi_f D_v\rho_m s}{P - hP^*}, \tag{13}$$

where H_v is the latent heat of vaporization of water that was approximated by $45144 - 48T_c$ J/mol, h is the relative humidity, ϕ_f is a weighting function that quantifies the wetness of soil, D_v is the vapor diffusivity in air, ρ_m is the molar density of air. D_v and ρ_m are defined as:

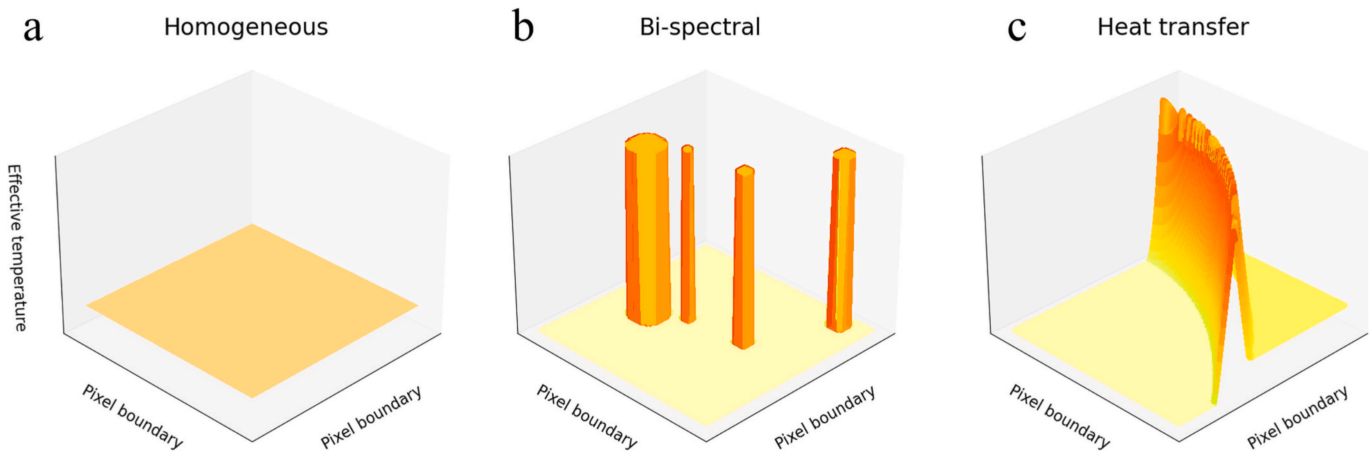

Fig. 1. Schematics of (a) homogeneous temperature model, (b) bi-spectral model, and (c) heat transfer model for retrieving the effective temperature variation functions in a fire pixel. The height of the surface plot indicates the magnitude of the retrieved temperature.

$$D_v = D_{vsat}\left(\frac{P_{sl}}{P}\right)\left(\frac{T}{T_{std}}\right)^{1.75}, \tag{14}$$

and

$$\rho_m = \rho_{m0}\left(\frac{P}{P_{sl}}\right)\left(\frac{T_{std}}{T}\right). \tag{15}$$

P_{sl} and T_{std} are sea-level pressure and standard temperature, respectively. D_{vsat} is the diffusivity at standard condition with a value of 2.12×10^{-5} m^2/s, and ρ_{m0} equals 44.65 mol/m^3. P^* (in Pa) is the saturation vapor pressure of water in soil pores, and s (in Pa/K) is the slope of the saturation vapor pressure versus temperature function. They are approximated by:

$$P^* = 101325 \bullet \exp\left(13.3815\hat{T} - 1.976\hat{T}^2 - 0.6445\hat{T}^3 - 0.1299\hat{T}^4\right), \tag{16}$$

and

$$s = 373.15 \bullet P^* \bullet \left(13.3015 - 4.082\hat{T} - 0.78\hat{T}^2 + 10.76\hat{T}^3\right)/T^2, \tag{17}$$

where $\hat{T}$ is a dimensionless temperature indicator that equals $1-(373.15/T)$. In Eq. (13), $1/(P-hP^*)$ is a term that represents the shift of vapor equilibrium when the soil moisture varies. The weighting factors for each soil component in Eq. (10), f_s, f_w, and f_a, have a uniform format of

$$f_i = \frac{x_i}{3}\left[\frac{1}{1+\left(\frac{\kappa_i}{\kappa_f}-1\right)g_a} + \frac{1}{1+\left(\frac{\kappa_i}{\kappa_f}-1\right)g_b} + \frac{1}{1+\left(\frac{\kappa_i}{\kappa_f}-1\right)g_c}\right], \tag{18}$$

where the subscript i refers to solid (s), water (w), and air (a). x_i is the volumetric fraction of soil component i. Under this definition, total porosity can be written as $x_w + x_a$, and air-filled porosity ω equals x_a. g_a, g_b, and g_c are three shape factors of soil. This study uses the same relationships described in De Vries and Van Wijk (1963), including: (1) the sum of three shape factors equals to unity and (2) g_a equals g_b. Furthermore, κ_f is an effective thermal conductivity of fluid components that can be written as the weighted mixture of κ_a and κ_w. An interpolation function determines its magnitude by:

$$\kappa_f = \kappa_a + \phi_f(\kappa_w - \kappa_a). \tag{19}$$

The weighting factor ϕ_f in Eqs. (13) and (19) is computed by:

$$\phi_f = \frac{1}{1+\left(\frac{x_w}{x_{ws}}\right)^{-q}}, \tag{20}$$

$$q = q_0\left(\frac{T}{303}\right)^2, \tag{21}$$

where T is the temperature in Kelvin. g_a, x_{ws} (m^3/m^3) and q_0 are soil-specific properties that are empirically determined. This study used the suggested values of Palouse B type soil, which are 0.074, 0.230 (m^3/m^3), and 5.83, respectively (Campbell et al., 1994). ϕ_f ranges between 0 (dry soil) and 1 (saturated soil). Due to a faster change of ϕ_f value than relative humidity h, h can be regarded as constant unity.

The advection parameters in the right side of Eq. (9) were expressed as: c_p was set to be 1010 J/(kg • K) and was insensitive to variation of temperature and soil moisture, ρ_a (in kg/m^3) was computed from air molar density ρ_m which was defined in Eq. (15). The effective advection velocity of soil air beneath the land surface, $\vec{u_v}$, was assumed to be outward from fire to represent a near-stagnant condition. The numerical model parameters outlined in this section were incorporated into Eq. (9) to retrieve the temperature functions. Given the heat transfer process and a resulting temperature variation pattern near the wildfire, Eq. (4) (Eq. (5) equivalently) should be further modified to:

$$L_4 = \left(\frac{1}{S_{\text{pix}}}\right)\iint \tau_4[e_4 B(\lambda_4, T(x,y))]\mathrm{d}x\mathrm{d}y, \tag{22}$$

where the integral domain in Eq. (22) is the entire fire pixel. The algorithm was run repeatedly with input fire peaked temperature and fire fronts' location pairs to generate radiances at 4 μm (11 μm equivalently). The input fire parameter pair with the least radiance deviation from the observation was output as the retrieval result. After obtaining the peaked fire temperature and the associated temperature function from the fire center to the pixel edge, this algorithm further assumes the area that has a retrieved effective temperature higher than the background as the fire area.

4. Model sensitivity to the fire parameters

4.1. Factors that affect the retrieved temperature function

The governing advection-diffusion equation resolves the functions that represent the retrieved temperature variations. Those functions are continuous and differentiable everywhere except for the location of peaked temperature. Fire size, or the fraction of fire area in each pixel, is mainly constrained by the shape of temperature functions and the relationship between the retrieved temperature function and the threshold of fire temperature. This section discusses these significant factors. Fig. 2a demonstrates the sensitivity of retrieved temperature functions to varied fire peaked temperature (from 600 K to 1400 K). The fire pixel has a cool background temperature of 304.5 K and a fixed effective advection velocity of 10 m per day. Fire sizes are measured by the areas with a retrieved temperature higher than the background temperature. This figure indicates that fire size grows as the fire peaking temperature increases when other environmental parameters are fixed. Fire temperature and size are mutually dependent.

Curves in Fig. 2a are plotted based on an assumption of near-stagnant advection velocity. However, the magnitude of advection velocity is highly varied in different ambient conditions, and it sensitively affects the temperature descending slopes like the peaked temperature. Fig. 2b demonstrates that temperature drops faster from the fire center (with a fixed temperature of 1200 K) to pixel edges (with a cool background temperature of 304.5 K) as the effective advection velocity increases (the function curves from the outermost to the innermost in Fig. 2b represent scenarios of 1, 2, 5, 10, and 100 m/day, respectively). When the peaked fire temperature is fixed, the ascending advection velocity of soil air results in a shift of fire fronts towards the fire center, and the retrieved fire area is thereby shrinking compared to a more stagnant condition.

4.2. *Sensitivity of the radiances at 4 and 11 μm bands to the variations in fire parameters*

Traditional bi-spectral methods independently retrieve fire temperature and the fraction of fire area in a single pixel. The radiances uniquely determine the temperature-area pair at 4 and 11 μm bands with known surface reflectance and atmospheric transmittance. As stated in the previous section, the two independent factors of the heat-transfer retrieval algorithm that determine the temperature variation functions are peaked fire temperature and effective advection velocity. From this perspective, the temperature-velocity pair can also be interpreted as a temperature-area pair.

In Fig. 3, we show the sensitivity of the brightness temperatures at 4 (BT_4) and 11 μm (BT_{11}) bands to the variations of peaked fire temperature T_f and effective advection speed u_v. This specific example corresponds to the lookup table for a fire pixel detected by GOES-16 satellite at 21:07 (UTC) on August 3, 2019. The kinetic background temperature is assumed to be identical to the BT_4 of the surface background, which is 305.617 K. The observation has a satellite zenith angle of 69.5° and a solar zenith angle of 32.9°. Dashed lines represent the observed radiant temperature pairs at 4 and 11 μm given a fixed effective advection velocity (in meters per day), while the solid lines represent the temperature pairs given a constant peaked fire temperature (in Kelvin). T_f increases from kinetic background temperature to 900 K. Each solid line is spaced at intervals of 100 K starting from 400 K in this figure, while the upper and lower limits of the effective advection velocities are 100 and 1 m per day, respectively. Note here that all dashed lines originate from the same bottom-leftmost point, representing that the peaking temperature equals the kinetic background temperature.

This figure shows that increases in T_f and decreases in u_v can cause higher brightness temperatures in both bands. The inset of Fig. 3 highlights the BT_4 and BT_{11} responses to the variations of T_f and u_v in a more flowing or moving condition (high u_v conditions). The varied lengths of dashed lines indicate that the same T_f increases always lead to a weaker brightness temperature change in those less stagnant environments. In other words, higher radiance measurement accuracy is required to retrieve fire peaking temperature in a less stagnant environment. Similarly, from the lengths of solid lines, we learn that at a higher T_f level, brightness temperature pairs change into a broader range as u_v changes. Besides, the slopes of dashed and solid lines ($\delta BT_4/\delta BT_{11}$) are interpreted as the relative change in BT_4 to BT_{11} due to the variations of T_f and u_v, respectively. Each dashed line starts with an ascending $\delta BT_4/\delta BT_{11}$ value as T_f increases from the background temperature point. As T_f continuously increases, especially for those more stagnant conditions, the slope value gradually stops to increase and then decreases. This pattern implies that in the lower u_v region, the same δBT_4 corresponding to the linearly elevated T_f is first matched to a descending δBT_{11} until a local minimum, and then δBT_{11} amplifies again.

5. Applications of the heat-transfer retrieval algorithm

The present study applied the fire-area retrieval algorithm to the data detected by GOES-16/17 satellites during the FIREX-AQ field campaign (Warneke et al., 2023). In this section, the retrieval outputs are evaluated against the observations from other platforms. Continuous and comprehensive observations of wildfires and small-scale agricultural fires were conducted in multiple locations in the United States during the summer of 2019 through ground-based measurements, aircraft surveys, and satellite remote sensing. Williams Flats fire was the largest sampled fire during the FIREX-AQ campaign. Lightning strikes ignited it on August 2 and was entirely contained by August 25, with a total burned area of over 44,000 acres. FIREX-AQ observations collected over the William Flats demonstrated that fire energetics correlated to the

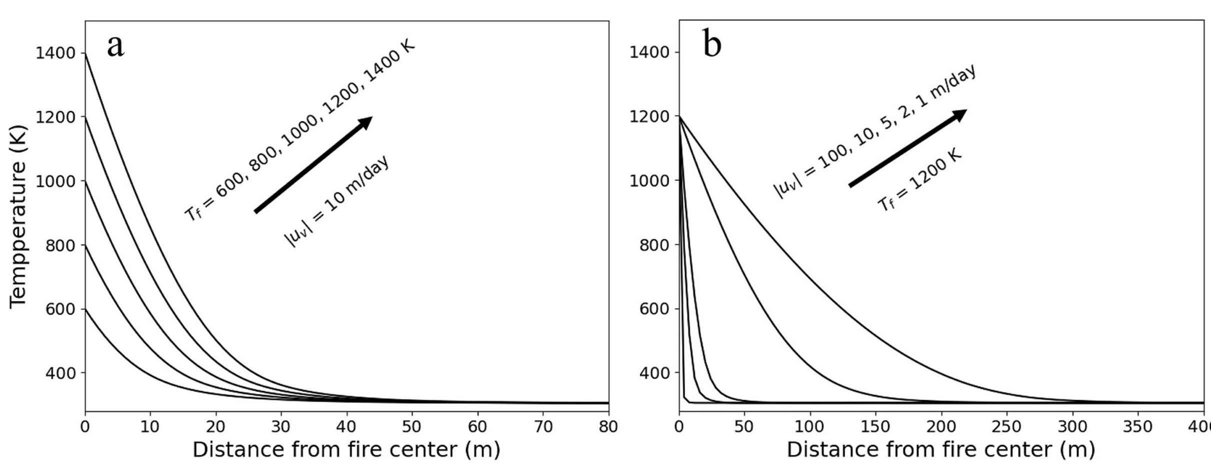

Fig. 2. Sensitivity of the retrieved subpixel temperature function to different (a) peaked fire temperature and (b) effective advection velocity. In (a), the function curves from the innermost to the outermost represent the retrieved temperature variations with a peaked fire temperatures of 600, 800, 1000, 1200, and 1400 K and a constant effective advection velocity of 10 m/day, respectively. In (b), the function representations from the innermost to the outermost show the retrievals with different effective advection velocities of 100, 10, 5, 2, and 1 m/day and a fixed peaked fire temperature at 1200 K, respectively.

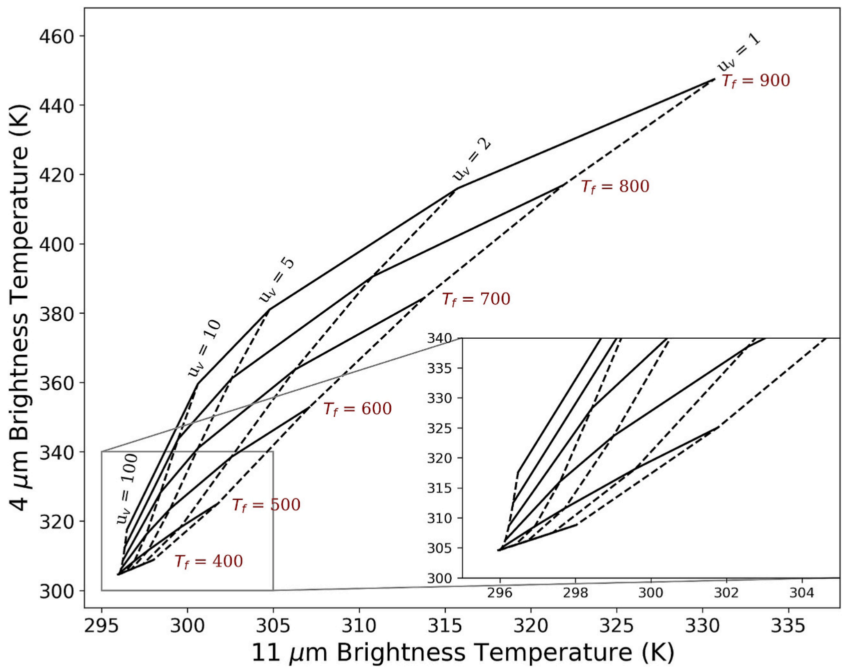

Fig. 3. Sensitivity of the brightness temperature at 4 and 11 μm bands to variations in peaked fire temperature T_f (in Kelvin) and effective advection velocity u_v (in meters per day).

relative trend in conserved smoke tracers (Wiggins et al., 2020, 2021). Besides, satellite and aircraft measurements have observed the occurrences of pyro-cumulonimbus cloud (pyroCb), which can modify local weather patterns and precipitations and potentially cause perturbations in stratospheric composition over the fire-affected region several days after the fire started (Peterson et al., 2022). Accurate inversion of the fire area and fire energetics is of great significance for estimating fire emissions and wildfire energy release, as well as further studying the driving forces of phenomena such as pyroCb. To study Williams Flats fire in this section, we utilized remote sensing data from both geostationary and polar-orbiting satellites to show the diurnal variations of fire intensity and the progression of fire perimeters. Then, a new set of FRP and associated fire parameters were obtained by applying the proposed retrieval method to high-temporal-resolution GOES observations and compared with those from collocated VIIRS active fire products Besides, the new GOES-based FRP data are evaluated against the observations from high-spatial-resolution ($\sim$ 30 m) MASTER aboard NASA DC-8 aircraft. MASTER provides more reliable references for fire-emitted radiances and other derivative parameters from a closer distance during the campaign. Finally, since the proposed algorithm outputs a complete temperature function for each fire pixel, it is possible to partition the flaming and smoldering regions by applying a "temperature threshold" on the variation function. This additional information will shed light on accurately assessing the emission rates of pollutants under different combustion conditions.

5.1. Progression of Williams flats fire

Williams Flats fire was first spotted on August 2, 2019. Its intensity exhibits a strong diurnal variation pattern, which is quantified by FRP. The cycle starts to develop near local noon and reaches its maximum in the afternoon. Most observed fire diurnal cycles diminish after sunset, although some strong and large-scale fires can still emit detectable energy in the late night (Wiggins et al., 2020). High-temporal resolution FRP data can be used to retrieve fire emissions and other important fire parameters. They are obtained from observations from geostationary Earth orbit (GEO) satellites.

The FRP diurnal cycles of Williams Flats Fire are depicted in Fig. 4a as time-series of FRP. Fire diurnal cycles on each day can be approximated by a mixture of monomodal and multimodal patterns. The modal peaks generally appear in the local afternoons. In Fig. 4b, we further demonstrate how the fire spreads geographically using polar-orbiting satellites observations that provide finer spatial resolution data. The data of fire hot spots used here were detected by VIIRS aboard the S-NPP satellite. The different colour dots in this figure represent all the fire pixels the radiometer observed on the corresponding dates. This figure shows that the Williams Flats Fire spreads northwards and eastwards due to a combination of factors, including terrain, surface vegetation covers, and dominant wind directions.

5.2. Comparisons of GOES FRP with collocated VIIRS FRP

Due to polar-orbiting satellites passing over the same area only twice a day, the observed fire area between two consecutive days shows noticeable discontinuities in Fig. 4b, especially during the beginning stage of the fire. The VIIRS 375-m active fire product has a spatial resolution of 375 m, with an effective footprint ranging from the nominal 375 m resolution (383 $\times$ 360 m) at the sub-satellite point to 795 $\times$ 784 m at a maximum scan angle of 56.28°. In this study, the VIIRS fire pixels we selected fall within an area range of 0.15 to 0.63 km^2. During the active burning period of the Williams Flats fire that we studied, a total of 2106 individual VIIRS fire pixel observations were obtained. The I4 band was saturated in 240 detected pixels among all the observations, though it had negligible impacts on the performance of M13 band, and thereby our acquisition of FRP data. The studied fire is located at the nadir point of the S-NPP at approximately 1:30 pm and 1:30 am (local time). In this study, we used the fire pixel data observed at those off-nadir angles as well. The uncertainty in FRP retrieval caused by viewing angles will be investigated in the future work. Besides, the variation of the atmospheric column water content at different times of the day can affect the transmittance of the infrared radiation. The VIIRS fire pixels used in this study were detected between 12:30 pm – 3:00 pm (daytime) and 1:00 am – 4:30 am (nighttime). The observational data of the vertical profile of water vapor can be further incorporated into the radiative transfer simulation to obtain more reliable retrievals of fire parameters.

Although VIIRS provides high spatial resolution fire detection, the

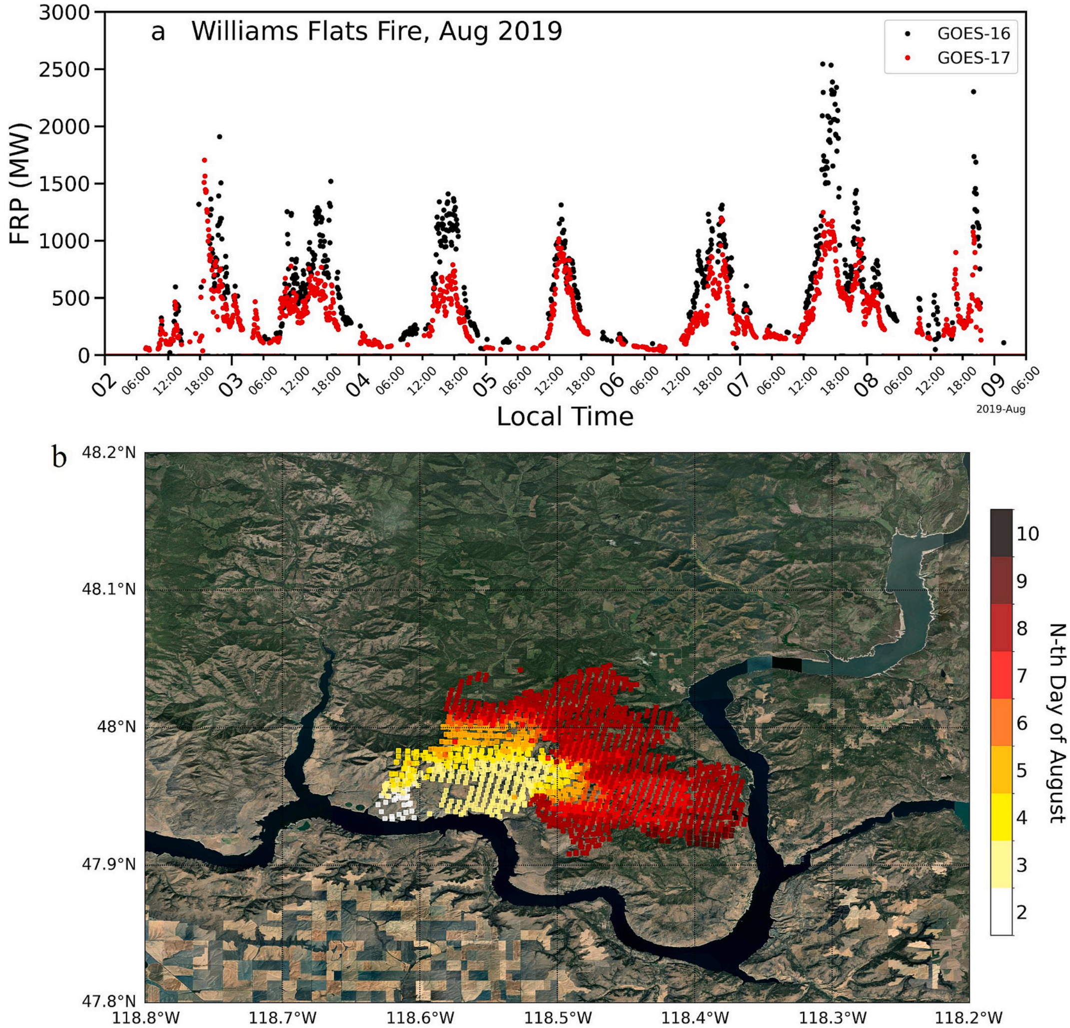

Fig. 4. The 2019 Williams Flats fire activities observed by satellite platforms during the FIREX-AQ campaign. (a) The diurnal cycles of the FRP retrieved from the observations by ABI aboard GOES-16 (black dots) and 17 (red dots) satellites. (b) The progression of the fire area observed by VIIRS aboard the S-NPP satellite. (For interpretation of the references to colour in this figure legend, the reader is referred to the web version of this article.)

rapidly changing nature of wildfires makes geostationary satellite data particularly valuable for studying real-time wildfire intensity. Here, we mainly applied the retrieval algorithms on the GOES datasets during the active period of the Wiliams Flats fire (Aug 2 to Aug 9, 2019) and first compared the subpixel retrievals with the collocated VIIRS observations. The pixel areas of GOES-16 and GOES-17 in the Williams Flats fire region are approximately 20 km^2 and 9 km^2, respectively. 77 and 135 collocated fire pixels are captured by ABI aboard GOES-16 and 17 during the studied active fire period of the Williams Flats fire, respectively. The retrieved pixel-based FRP and fire area are then computed for further comparison.

Pixel-based FRP of heat-transfer algorithm FRP_{HF} is obtained according to the Stefan-Boltzmann relationship by,

$$FRP_{\mathrm{HF}} = \int \sigma\left(T(s)^4 - T_b^4\right)ds, \tag{23}$$

where $T(s)$ is the retrieved temperature over the fire region s. This FRP value is firstly compared with the FRP obtained by the single-band MIR approach through the WFABBA algorithm. Fig. 5a and b show the correlations between two types of FRP from GOES-17 and 16 satellites, respectively. More fire pixels were captured by GOES-17 than 16 mainly because of its smaller viewing zenith angle and, thereby, smaller pixel size over the fire region. It was found that the FRPs computed by heat-transfer algorithm fit better with the ones obtained by the MIR method in those GOES-17 fire pixels ($R^2 = 0.649$) than GOES-16 counterparts. The scaling factor between the two types of FRP in GOES-17 cases is very close to the 1:1 reference line. The p-value (0.103) here indicates that the correlation is not statistically significant at the typical 0.05 level. Several factors could lead to this result. For example, the collocated fire pixels between the two selected active products for the Williams Flats fire event are not enough to exhibit a significant linear correlation, and fires may show inconsistent burning activities during the daily time window when the two sensors have overlapped measurements.

In Fig. 5a and b, the colour of each data point represents the background temperature at 4 μm. The heat-transfer method generally outputs lower FRP values for those observations with a cooler background temperature. By plotting the background temperatures of all detected fire pixels versus the local time in Fig. 5c and d, we observed that these temperatures exhibit a strong diurnal variation pattern during the active period of the fire. Observations with a cooler background temperature in Fig. 5a and b are associated with a nighttime or early morning sampling time.

Two consecutive GOES measurements with an interval of ten minutes are synchronized with the VIIRS observation if their time interval covers the acquisition time of the associated VIIRS observation. As we stated in section 2.4, we conducted collocation analysis of VIIRS and GOES FRP at both pixel and cluster level. For the pixel-based

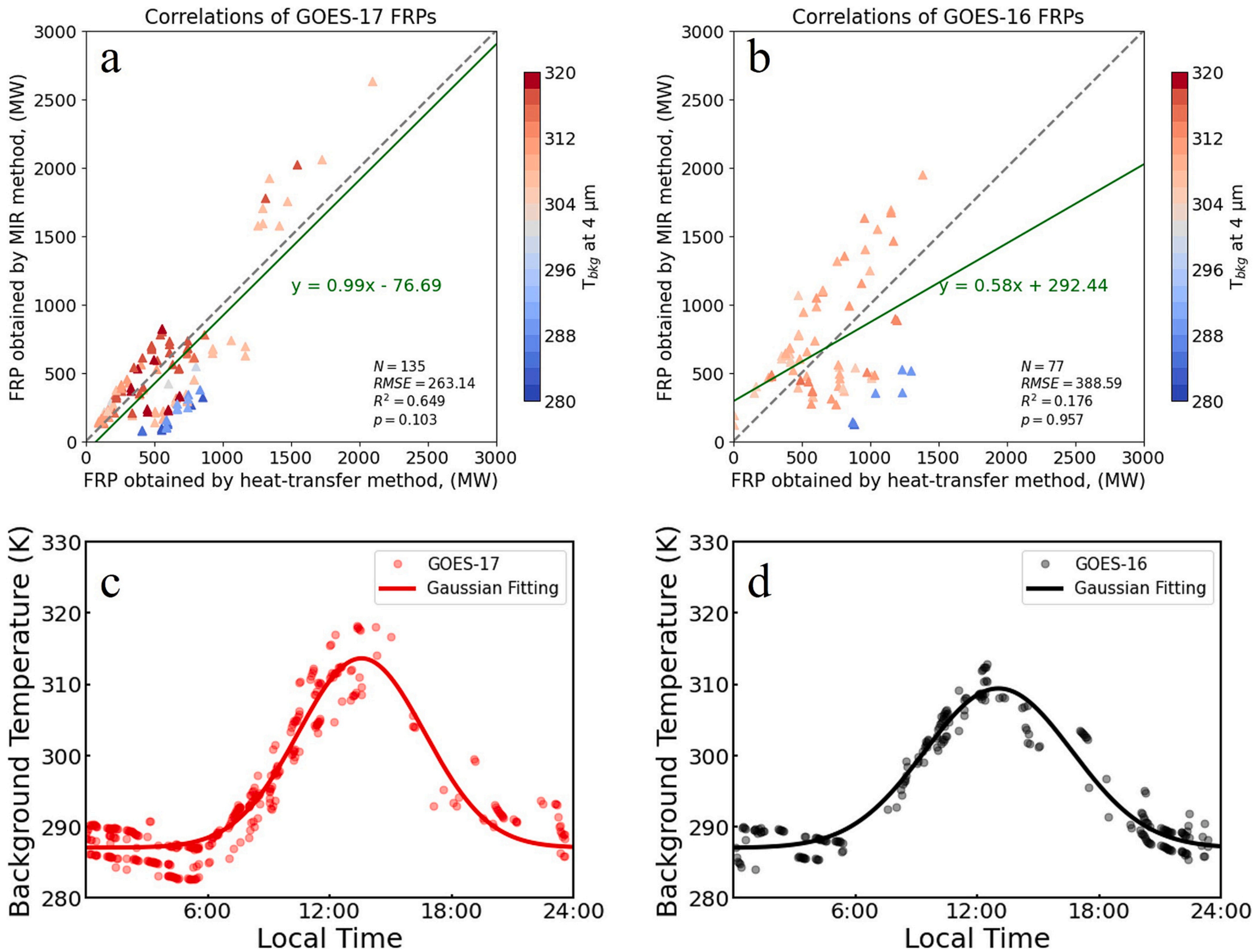

Fig. 5. Correlations between the FRPs obtained from the heat-transfer algorithm and the single-band MIR method (in the released WFABBA products) from (a) GOES-17 and (b) 16 observations, respectively. The grey dashed lines represent the line of equality, indicating where the FRP values calculated by the two methods are identical. (c) and (d) show the diurnal cycle of the background brightness temperature of all fire pixels detected by GOES-17 and 16, respectively.

comparison, the correlation relationship between GOES-17 and collocated VIIRS pixel-based FRP is shown in Fig. 6a and b. Cases with a zero VIIRS FRP value are first filtered. Most of the aggregated VIIRS FRP is about or less than half of the collocated GOES FRP in magnitude. Combining the results of the R-squared and *p*-value, we found that the moderate correlation between GOES FRP obtained through the heat-transfer method and VIIRS FRP is statistically significant among the collocated pixel-based FRP cases of the Williams Flats fire we studied. In contrast, although the MIR method yields a stronger linear correlation, this relationship is not statistically significant. On the other hand, we've conducted correlations analysis of cluster-based FRP in Fig. 6c and d. Due to the clustering of fire pixels, the number of collocated FRP cases used for comparison is smaller than that of pixel-based FRP. Similar to the correlation observed with pixel-based FRP, the GOES FRP derived from the heat-transfer method shows a slightly weaker linear relationship with VIIRS FRP compared to the MIR method, but this relationship is more statistically significant.

5.3. Comparisons of GOES FRP with collocated MASTER FRP

Suborbital observations of the Williams Flats fire are another important data source that can be compared with the FRP retrievals from remote sensing platforms. MASTER aboard DC-8 aircraft provided FRP data on August 3, 6, 7, and 8 (local solar time). On these four days, the aircraft circled multiple times over the fire regions, offering relatively complete geographical coverage of the active fire area. Besides, due to the closer distance between the imager and the fire, the atmospheric attenuation and the received radiance uncertainty caused by the viewing zenith angle are significantly reduced. All those factors make MASTER-retrieved FRP a more reliable validation set than those from polar-orbiting satellite platforms. Fig. S1 illustrates the vertical profile of the backscattering coefficients at 532 nm measured by High Spectral Resolution Lidar (HSRL) aboard DC-8 aircraft during the Williams Flats fire. The black lines in each figure indicate the flight altitudes of DC-8. The starting and ending time of each DC-8 flight (UTC) and the dependency of MASTER pixel size on flight altitude are shown in Table S1. The MASTER data used for further analysis has a pixel resolution ranging from 15 to 30 m.

The derivation of FRP from MASTER observations is based on a similar single-band MIR approach as stated in the previous sections. Like the process of correlating VIIRS FRP to two types of GOES FRP, we first identify the collocated pixel-based FRP from the products of MASTER and GOES by combining the use of the ray casting algorithm and temporal averaging of multiple synchronized GOES pixel-based FRPs. The scatter points in Fig. 7 represent all the detected fire spots by MASTER of four time periods (01:13–01:17 am, 01:20–01:21 am, 02:04–02:06 am, and 02:19–02:26 am, Aug 9 (UTC)). Since the MASTER observations coincided with an active pyroCb event, the dense convective clouds

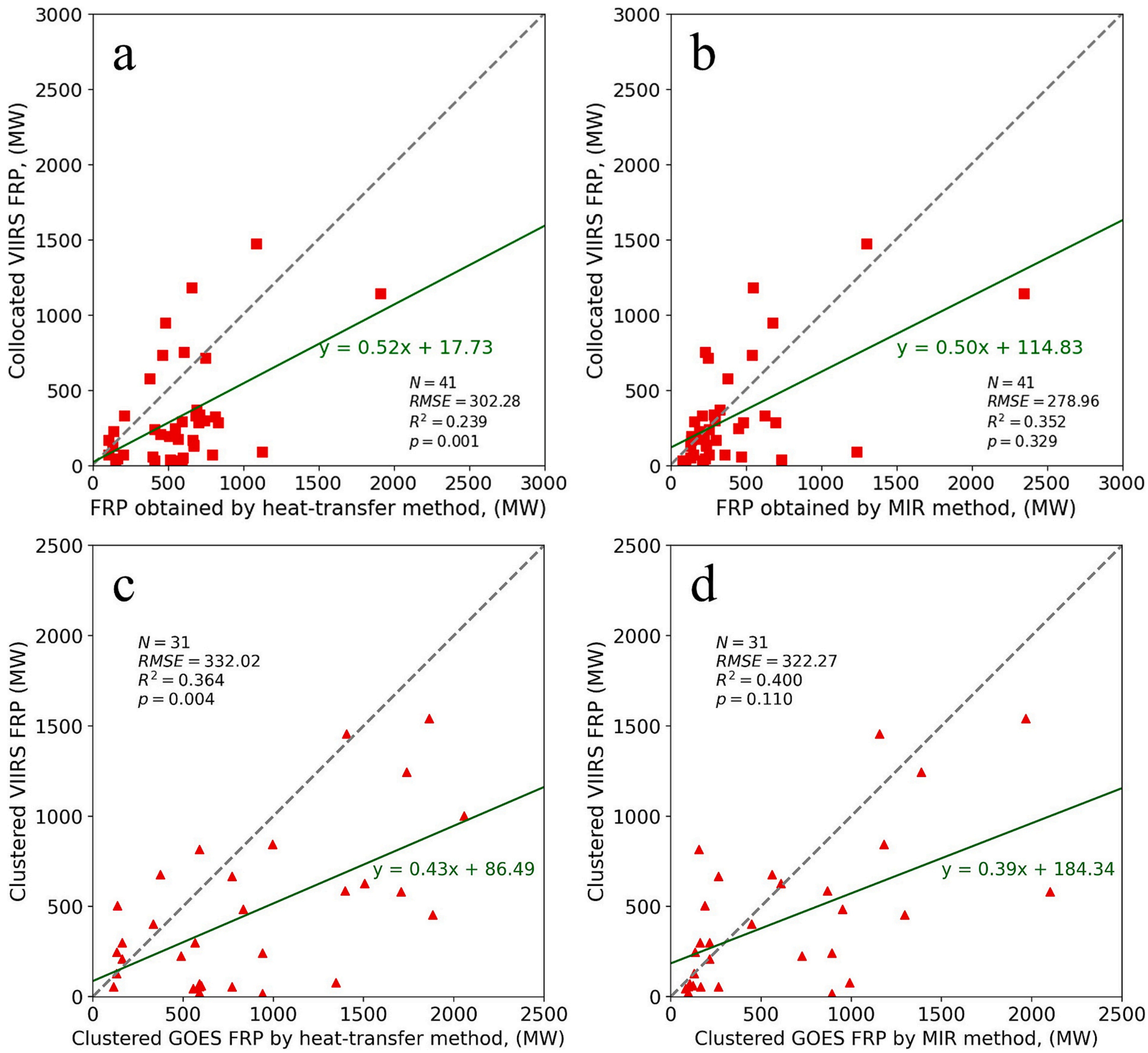

Fig. 6. Correlations between the VIIRS FRP and the collocated pixel-based GOES-17 FRPs obtained from (a) the heat-transfer algorithm and (b) the MIR method. (c) and (d) are correlation between the cluster-based VIIRS FRP and collocated GOES-17 FRPs obtained from the two retrievals methods.

caused some fire signals to be missed by the ABI imager aboard GOES satellites. The identified combustion types are labeled as different colors. This figure shows that most active fire areas were under smoldering combustion conditions, and almost all isolated fire regions were comprised of a mixture of flaming and smoldering areas. Saturated fire pixels account for only a very small portion. The areas classified as flaming combustion are mainly located at the periphery of the fire region, which is in accordance with the pattern of fire front propagation. The polygons of collocated GOES-16 and 17 fire pixel footprints are drawn in blue and magenta, respectively. The fire pixels in Fig. 7 were captured by GOES at 01:21 am.

Like the correlation analysis for VIIRS FRP, we computed the linear regression statistical metrics between FRPs computed by the heat-transfer method and those retrieved by the MIR method. As shown in Fig. 8a and b, GOES-17 cases show a stronger linear correlation ($R^2 = 0.726$) between two types of GOES FRP than the GOES-16 observations ($R^2 = 0.639$). The slope of the fitted line for GOES-17 cases is also closer to one, implying that the two types of FRP are comparable in magnitudes. The *p* value of the linear correlation of GOES-16 FRP obtained by MIR and heat-transfer method is 0.277, which implies their correlation is not statistically significant. Fig. 8b also shows that as the pixel-based FRP values increase, the linear relationship between the GOES-16 FRP calculated by the two methods becomes stronger. According to the collocation analyzes of GOES-VIIRS retrievals in Fig. 5 and those of GOES-MASTER retrievals in Fig. 8, We found that GOES-17, due to its finer spatial resolution over the Williams Flats fire area than GOES-16, results in smaller deviations between the FRP calculated using the heat-transfer method and the traditional MIR method. The FRP of fire pixels with higher background temperatures that were retrieved using the MIR method tends to be slightly higher than the FRP calculated using the heat transfer method, while the opposite is true for pixels with lower background temperatures. Since the GOES FDC also provides fire area and temperature retrievals using the Dozier method, we can therefore calculate pixel-based FRP based on Eq. (1). As shown in Fig. S2, the FRPs computed by Dozier's bi-spectral method show a quite strong linear correlation with those computed by MIR method. In contrast, the FRP computed by the proposed heat-transfer method shows a weaker correlation and a slope deviates from unity. Overall, the main reason for a less statistically significant correlation of using the heat-transfer method is that all three FRP calculation methods covered in this study fundamentally rely on the necessity to use a fourth-order power law approximation to Planck's radiation function. This approximation works well in the temperature range between 600 K and 1600 K (Wooster et al., 2003). What sets it apart from the other two methods is that the

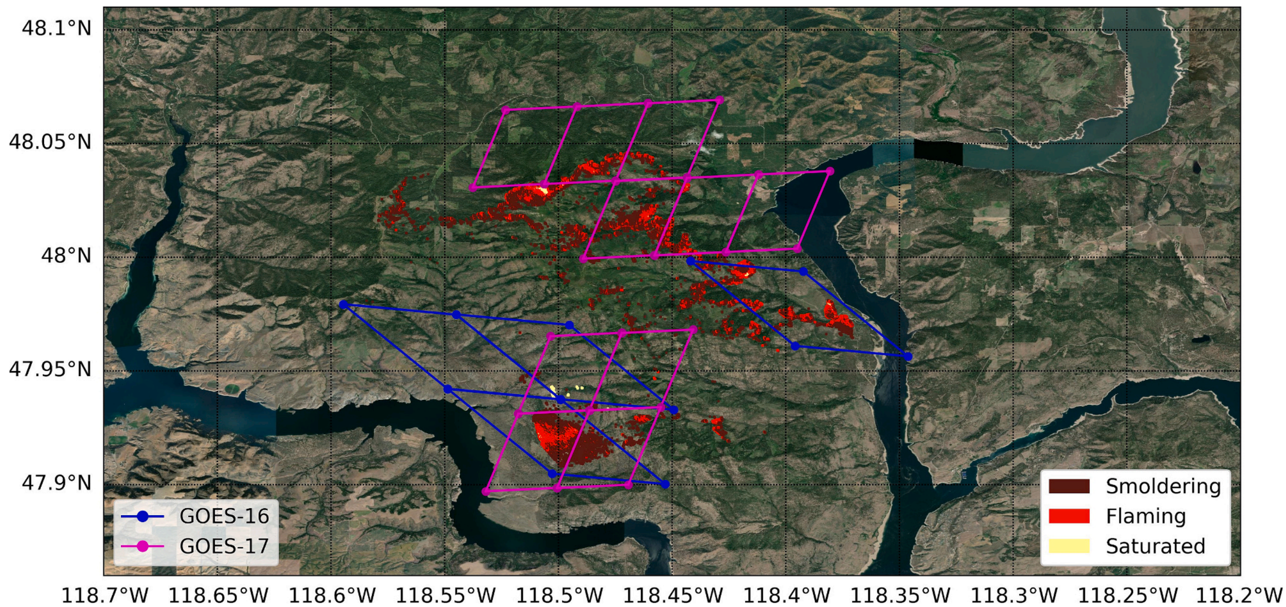

Fig. 7. All fire spots detected by MASTER between 01:13 am and 02:19 am (UTC) on Aug 9, 2019. The fire spots labeled as "Smoldering", "Flaming", and "Saturated" based on their retrieved FRP values are shown in maroon, red, and yellow, respectively. Quadrilaterals in this figure outline GOES-16 (blue) and 17 (magenta) synchronized pixel footprints at 01:21 am. (For interpretation of the references to colour in this figure legend, the reader is referred to the web version of this article.)

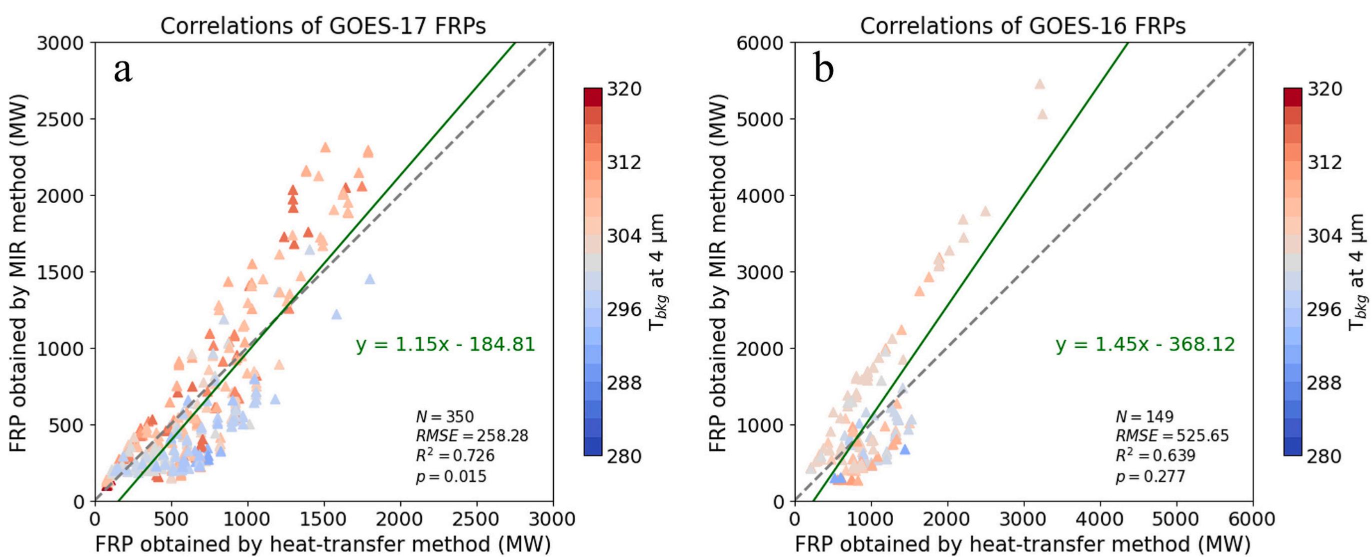

Fig. 8. Similar to Fig. 5a and b, this figure displays the two types of GOES FRPs retrieved for pixels with collocated MASTER observations.

heat-transfer method retrieves a temperature variation function that transitions continuously from the retrieved peaked fire temperature to the non-fire background temperature to calculate FRP. When integrating the temperature curve over lower temperature regions, this can introduce numerical deviations compared to the bi-spectral method or the MIR method, which do not account for temperature variations in those lower temperature ranges.

About 2 % of the MASTER fire pixels were labeled as saturated pixels. We removed them from the following correlation analysis because it is difficult to estimate FRP based on inaccurate brightness temperature. By further correlating the GOES-17 FRP to the collocated MASTER FRP in Fig. 9c and comparing it with Fig. 6a and c, we demonstrate that GOES FRP obtained through the heat-transfer method show a stronger linear correlation to the associated MASTER FRP than the collocated VIIRS FRP. Besides, comparisons between Fig. 9c and d show indicate a better correlation of GOES FRP retrieved by heat-transfer algorithm with the MASTER FRP retrievals than those obtained by MIR method.

5.4. *Retrievals of the fire area, FRP flux, and forms of combustion*

This study considers all subpixel areas with temperatures above the pixel's background temperature as retrieved fire areas. Fig. 10a shows the computed FRP against the fire area obtained through the heat-transfer algorithm. The values of FRP per pixel are mainly concentrated between 10^5 kW and 10^6 kW, with a corresponding retrieved fire area between 0.3 km^2 and 3 km^2. A power-law relationship positively correlates FRP and fire area per pixel ($FRP = 40.7531 \bullet Area^{0.673}$). Unlike the FRP flux obtained by dividing the single-band MIR FRP by the entire pixel area in Fig. 4a, here we can use the FRP, calculated by excluding the background radiation contribution, along with the corresponding fire area, to determine the actual FRP flux of the fire.

Given that the exponent of the area in the power-law relationship is

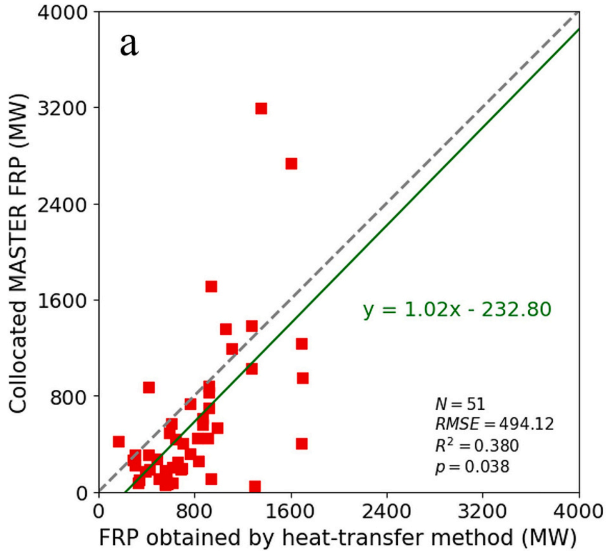

Fig. 9. Similar to Fig. 6a and b, but this figure correlates the two types of GOES-17 FRPs with the FRP retrievals from the MASTER observations.

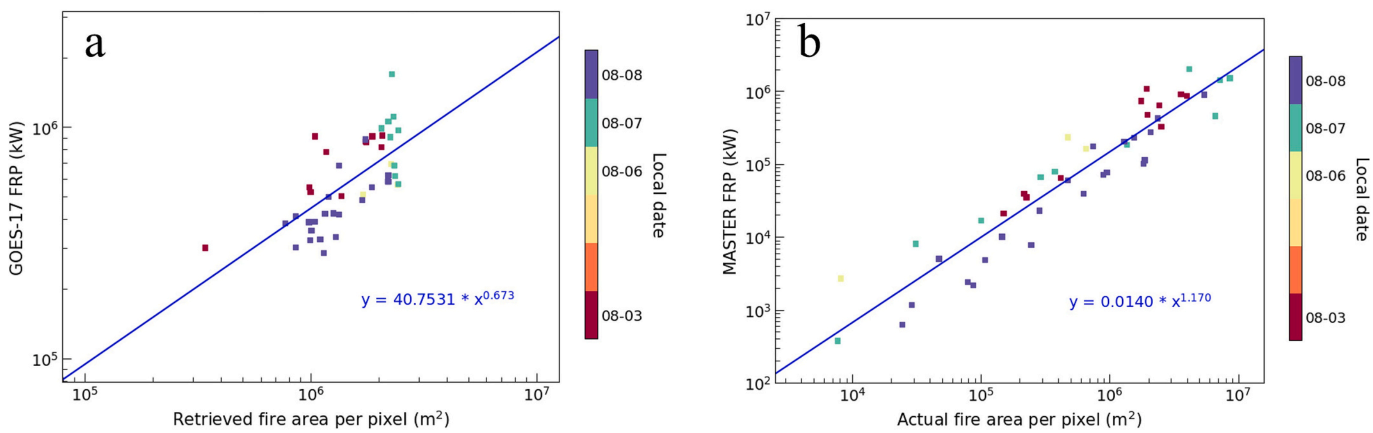

Fig. 10. Relationship of FRP and fire area under all combustion conditions (a) retrieved by heat-transfer algorithm and (b) detected by the MASTER instrument. The blue lines show the results of the power-law regression with the specific regression formula. The colors of the scatter points represent the corresponding observation dates in the local time zone. (For interpretation of the references to colour in this figure legend, the reader is referred to the web version of this article.)

less than one, FRP flux is inversely correlated with the retrieved fire area (FRP flux$\propto$Area$^{-0.327}$). In Fig. 2, we showed that the increased retrieved area in the heat transfer algorithm is due to either the rise of the maximum fire temperature or the decrease of effective advection rate, constrained by the overall pixel radiances. Fire area increases resulting from fire temperature rise tend to amplify the FRP flux, while the advection rate decreases pose an opposite effect. The negative correlation between FRP flux and the fire retrieved by GOES-17 observations implies that the area changes are dominated by advection rate.

The correlations between FRP and actual fire area in the coincident GOES fire pixels detected by the airborne MASTER instrument are shown in Fig. 10b. The spatial resolution of MASTER observations depends on the average flight altitude. We only selected the measurement data from the stable flight phase for the subsequent analysis, corresponding to a spatial resolution of 20 to 30 m. The fitted power-law relationship between FRPs and observed fire areas in Fig. 10b has an exponent that is a bit above one, indicating the FRP fluxes measured by MASTER have a weak positive correlation with fire area. Meanwhile, the MASTER-detected FRP and fire area have a more comprehensive range of values. It reflects that the realistic fire propagation and the shape of active fire fronts are more diverse than the assumptions of the heat-transfer model. Our future model can be improved by considering the spatial relationships between the objective fire pixel and the nearby precedent fire pixels.

Compared to the bi-spectral method, another notable feature of the proposed heat-transfer method is its ability to retrieve the continuous temperature variations within the fire pixel. Areas under different combustion conditions within a GOES pixel can be determined by assigning a “cutoff” value to the retrieved fire variation function. This temperature-based classification principle is similar to the one applied to the MASTER observations. A MASTER fire pixel is classified as under flaming or smoldering combustion when its 4-μm band brightness temperature is higher than three or two standard deviations above the background mean brightness temperature, respectively. Meanwhile, this hotter-than-background pixel should satisfy other conditions, such as the brightness temperature difference between 4 and 11 μm bands, to be recognized as a flaming or smoldering pixel. Fig. 11a illustrates the probability density distribution of the MASTER-classified proportion of smoldering area in the total fire area in each GOES fire pixel. The area of the corresponding bar quantifies the frequency of smoldering fractions in each bin. It shows that the smoldering fraction has a major frequency peak at about 0.5 and a minor peak at 0.85, indicating that smoldering fire areas have comparable or larger sizes than flaming in most studied pixels. Brown carbon (BrC), mainly originates from the low-temperature

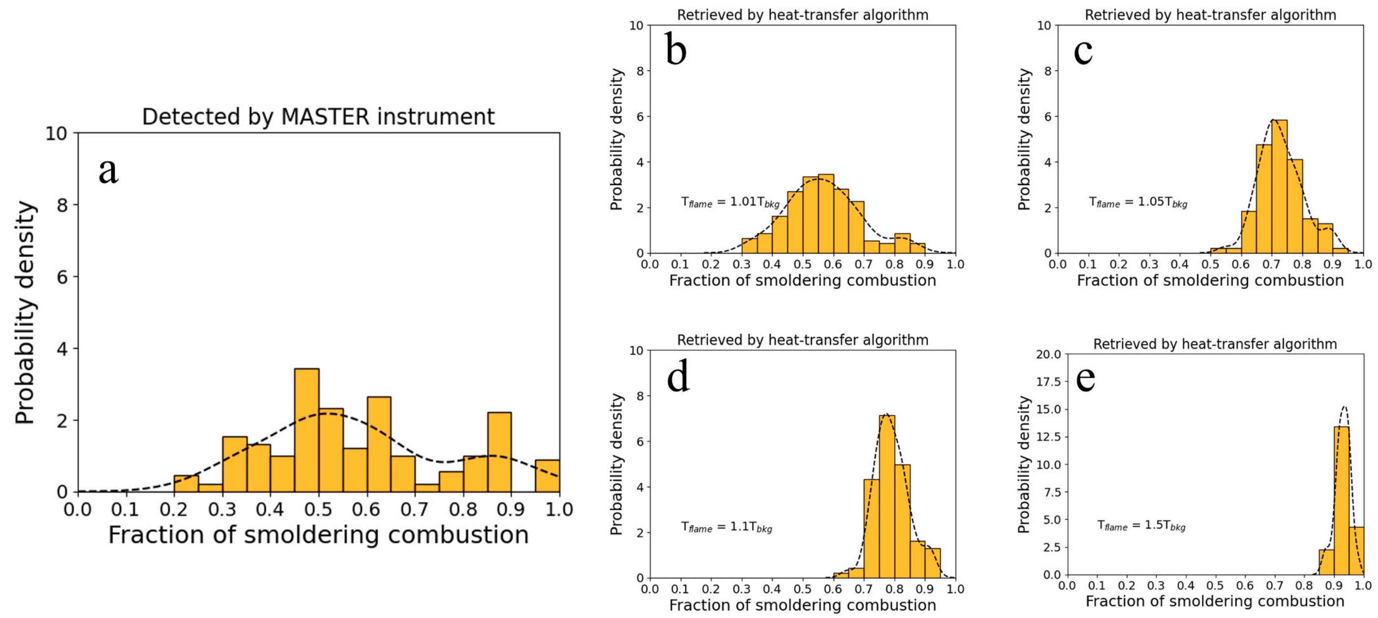

Fig. 11. (a) Density functions of the proportion of smoldering area in the total active fire area obtained by MASTER observations. (b), (c), (d), and (e) are retrieved smoldering fractions with a flaming temperature threshold of 1 %, 5 %, 10 %, and 50 % higher than the pixel's background temperature. The dashed line in each figure represents the fitting curve of the continuous probability density function.

combustion process, may play a dominant role in wildfire particulate emissions (Chakrabarty et al., 2023). The characterization of BrC from other particle species can be potentially conducted through the polarimetric remote sensing technique (Zhang et al., 2021).

Figs. 11b to 11e show probability density functions of retrieved smoldering area fractions with a cutoff temperature (T_{flame}) of 1 %, 5 %, 10 %, and 50 % higher than the GOES fire pixel's background temperature (T_{bkg}), respectively. We did not conduct a statistical analysis to determine the standard deviations of the background temperature of GOES fire pixels due to their much coarser spatial resolution and fewer background pixel samples. The areas with a temperature higher than the cutoff value are flaming areas, while the remaining fire areas are under smoldering combustion. As the rise of the selected cutoff temperature, smoldering combustion tends to increase its proportion in the total fire area. Besides, when the cutoff temperature is 1 % higher than the background temperature, the shape of the output density function is more consistent with the MASTER results.

6. Summary and conclusion

Fire radiative power (FRP) and subpixel fire properties, including fire temperature, fire area, and combustion phases in a fire pixel, are essential parameters to (1) estimate the emission rates of pollutants, (2) infer the plume injection height, and (3) understand the driving forces of pyrocumulonimbus. In this paper, we proposed a method based on the first principle of heat transfer to retrieve these vital fire parameters at a subpixel level. The traditional bi-spectral approach utilizes the measurements of radiance at MIR and TIR bands. It assumes an identical temperature for all in-pixel fire areas to retrieve fire area fraction and temperature. This study uses the brightness temperatures of fire and non-fire background pixels at two IR bands from high-temporal-resolution GOES ABI as input to the proposed algorithm. It runs iteratively to find the optimal peaked fire temperature and effective advection velocity to produce consistent radiances with the observations. The two optimized parameters determine the shape of the continuously varying temperature functions from the fire center to the cool background in each fire pixel. FRP, active fire area, peaked fire temperature, and the proportions of smoldering and flaming were retrieved based on the temperature function.

FRP in this study was computed through the Stefan-Boltzmann relationship, which integrates the difference between the fourth power of the temperature function and the fourth power of the background temperature over the region of the fire pixel. The retrieved GOES-17 FRP using the heat-transfer algorithm shows a good linear correlation with those computed by the MIR approach. It implies the critical role of measuring 4 μm radiances in determining the FRP in the studied methods. Most of the selected fire pixels with a background temperature lower than 300 K output higher FRP values using this heat-transfer algorithm than the MIR method. The background temperature exhibits strong diurnal variations, so these low-background-temperature data correspond to early morning or nighttime observations. Fine-spatial-resolution data can be further used to assess the retrieval performance of fire parameters. In this study, we applied both the ray-casting algorithm and an unsupervised DBSCAN algorithm to find the collocated FRP at a pixel level and at a cluster level from the active fire products with different spatial resolutions, respectively. Although conducting cluster analysis reduces the sample size for FRP comparison, it can help reduce the mismatch in fire regions caused by differences in sensors' detection capacities, thereby improving the correlation between collocated FRP. Moderate linear correlations were found between the pixel-based GOES FRP and the aggregated FRP from two other observational platforms. The correlation of GOES FRP derived from the heat-transfer algorithm with MASTER FRP is found to be more robust than with VIIRS FRP.

The retrieved temperature function curve can also obtain fire area and the fraction of different combustion phases. In the proposed retrieval framework, smoldering and flaming areas are partitioned by assigned characteristic temperatures. The MASTER measurements indicate that in most studied fire pixels, the smoldering area has a similar or even larger area compared to the flaming combustion area. Therefore, the combustion products from a relatively low fire temperature associated with smoldering conditions will account for a significant proportion of the total fire emissions. The FRP obtained by the heat transfer algorithm exhibits a power-law relationship with the retrieved fire area, while FRP flux is inversely correlated with the fire area. Though a similar power-law relationship between FRP and detected fire area has been quantified by the MASTER measurements, the MASTER FRP flux, on the other hand, shows a different dependency on the detected fire area. FRP flux, as a measure of the energy density released by wildfires per unit of time, is closely related to the real-time intensity of the fire, and it is also an important parameter for further studying plume dynamics. The deviation in the relationship between FRP flux and fire area derived by different methods indicates that FRP flux cannot be inferred from fire area alone, but should be linked to the diversity of vegetation types, terrain, and meteorological conditions at a finer resolution. Our proposed model shows the potential of resolving the subpixel-level features of a detected fire pixel, though it currently converts the heat transfer process that occurs in three-dimensional space to a one-dimensional direction and makes the assumptions to simplify the radiation process between the ground and the atmosphere This model can be further improved by explicitly incorporating the terrain, vegetation, and meteorological factors into the heat-transfer equation solving process. For example, by further utilizing land cover data products such as the combined MODIS International Geosphere-Biosphere Programme (IGBP) data, we can gain insights into the different types of vegetation (e.g., forest, grassland, savanna, etc.) and fuel availability within each pixel cell. Further incorporating the heat transfer properties of different land cover types into the model will help enhance its ability to retrieve the subpixel properties of wildfires. With increases in collocated observation cases, especially in situ measurements of wildfires, our knowledge of understanding the properties of subpixel fires will be further improved. The assumption of the fire perimeter geometry in the current model is more applicable to large-scale wildfires than to smaller or confined fires. In our future work, by analyzing the time series of the developments of the GOES fire pixels, we could get a better inference of the fire spread patterns, which would, in turn, improve the estimates of the actual fire perimeter geometry in each pixel and enhance the accuracy of model predictions. Additionally, the uncertainties caused by observational angles and the variations in atmospheric transmittance due to atmospheric water vapor content, which have not been addressed in this paper, will be reduced with more auxiliary measurement data. The retrieval model introduced in this article provides insights into the inversion of subpixel wildfire properties and the determination of fire-related parameters using high temporal resolution satellite data in the future.

CRediT authorship contribution statement

Chenchong Zhang: Writing – review & editing, Writing – original draft, Visualization, Validation, Software, Resources, Project administration, Methodology, Investigation, Formal analysis, Data curation, Conceptualization. **Yuan Wang:** Writing – review & editing, Resources, Project administration, Funding acquisition, Conceptualization. **Jun Wang:** Writing – review & editing, Methodology. **Amber Soja:** Writing – review & editing, Resources, Data curation. **Emily Gargulinski:** Writing – review & editing, Resources, Data curation. **David Peterson:** Writing – review & editing, Resources, Methodology, Data curation. **Olga Kalashnikova:** Writing – review & editing, Resources, Project administration, Funding acquisition. **Bin Zhao:** Writing – review & editing. **Yafang Cheng:** Writing – review & editing. **Fangjun Li:** Writing – review & editing. **Rajan Chakrabarty:** Writing – review & editing, Resources, Project administration, Funding acquisition, Conceptualization.

Declaration of competing interest

The authors declare that they have no known competing financial interests or personal relationships that could have appeared to influence the work reported in this paper.

Acknowledgments

Chenchong Zhang, Yuan Wang, and Olga Kalashnikova were supported by the Deep Space Climate Observatory (DSCOVR) project. This research has also been supported by the National Aeronautics and Space Administration (grant no. NNH20ZDA001N-ACCDAM), the National Oceanic and Atmospheric Administration (grant no. NA16OAR4310104), the National Science Foundation (grant nos. AGS-1455215 and AGS-1926817) and the US Department of Energy (grant no. DE-SC0021011). Chenchong Zhang was partially supported by the McDonnell International Scholars Academy at Washington University in St. Louis. NASA's Modeling, Analysis, and Prediction (MAP) Program (80HQTR21T0099) and the U.S. Naval Research Laboratory's 6.2 Base Program provided additional support for David Peterson. Olga Kalashnikova at the Jet Propulsion Laboratory, California Institute of Technology, under contract with the National Aeronautics and Space Administration, was also supported by the Compact Fire Infrared Radiance Spectral Tracker (c-FIRST) project.

Appendix A. Supplementary data

Supplementary data to this article can be found online at https://doi.org/10.1016/j.rse.2025.114871.

Data availability

The GOES-16/17 retrievals of the FIREX-AQ campaign were obtained from the NASA Airborne Science Data for Atmospheric Composition online repository (https://www-air.larc.nasa.gov/cgi-bin/ArcView/firexaq). The VIIRS Fire and Thermal Anomalies products were obtained from the NASA FIRMS platform (https://firms.modaps.eosdis.nasa.gov/active_fire/). The processed airborne FRP and combustion phases dataset were prepared by the MASTER team and are made available upon request.

References

Abatzoglou, J.T., Williams, A.P., 2016. Impact of anthropogenic climate change on wildfire across western US forests. Proc. Natl. Acad. Sci. 113 (42), 11770–11775. https://doi.org/10.1073/pnas.1607171113.

Andela, N., Kaiser, J.W., Van Der Werf, G.R., Wooster, M.J., 2015. New fire diurnal cycle characterizations to improve fire radiative energy assessments made from MODIS observations. Atmos. Chem. Phys. 15 (15), 8831–8846. https://doi.org/10.5194/acp-15-8831-2015.

Andreae, Meinrat O., 2019. Emission of trace gases and aerosols from biomass burning – an updated assessment. Atmos. Chem. Phys. 19 (13), 8523–8546. https://doi.org/10.5194/acp-19-8523-2019.

Andreae, M.O., Merlet, P., 2001. Emission of trace gases and aerosols from biomass burning. Glob. Biogeochem. Cycles 15 (4), 955–966. https://doi.org/10.1029/2000GB001382.

Bradstock, R.A., 2010. A biogeographic model of fire regimes in Australia: current and future implications. Glob. Ecol. Biogeogr. 19 (2), 145–158. https://doi.org/10.1111/j.1466-8238.2009.00512.x.

Brewer, M.J., Clements, C.B., 2019. The 2018 camp fire: meteorological analysis using in situ observations and numerical simulations. Atmosphere 11 (1), 47. https://doi.org/10.3390/atmos11010047.

Campbell, G.S., Jungbauer Jr., J.D., Bidlake, W.R., Hungerford, R.D., 1994. Predicting the effect of temperature on soil thermal conductivity. Soil Sci. 158 (5), 307–313.

Chakrabarty, R.K., Shetty, N.J., Thind, A.S., Beeler, P., Sumlin, B.J., Zhang, C., Liu, P., Idrobo, J.C., Adachi, K., Wagner, N.L., Schwarz, J.P., Ahern, A., Sedlacek, A.J., Lambe, A., Daube, C., Lyu, M., Liu, C., Herndon, S., Onasch, T.B., Mishra, R., 2023. Shortwave absorption by wildfire smoke dominated by dark brown carbon. Nat. Geosci. 16, 683–688. https://doi.org/10.1038/s41561-023-01237-9.

Csiszar, I., Schroeder, W., Giglio, L., Ellicott, E., Vadrevu, K.P., Justice, C.O., Wind, B., 2014. Active fires from the Suomi NPP Visible Infrared Imaging Radiometer Suite: Product status and first evaluation results. JGR-Atmos. 119, 803–816. https://doi.org/10.1002/2013JD020453.

Darmenov, A. and da Silva, A.: The quick fire emissions dataset (QFED) – Documentation of versions 2.1, 2.2 and 2.4. NASA//TM-2015-104606, Vol. 38, NASA Global Modeling and Assimilation Office, 183 pp., available at: https://gmao.gsfc.nasa.gov/pubs/docs/Darmenov796.pdf, 2015 (data available at: https://portal.nccs.nasa.gov/datashare/iesa/aerosol/emissions/QFED/v2.4r6/).

De Vries, D.A., Van Wijk, W.R., 1963. Physics of plant environment. In: Environmental Control of Plant Growth, 5, p. 69.

Dozier, J., 1981. A method for satellite identification of surface temperature fields of subpixel resolution. Remote Sens. Environ. 11, 221–229. https://doi.org/10.1016/0034-4257(81)90021-3.

Ester, M., Kriegel, H.-P., Sander, J., Xu, X., 1996. A density-based algorithm for discovering clusters in large spatial databases with noise. In: Simoudis, E., et al. (Eds.), Proc. Int. Conf. Knowledge Discovery and Data Mining. AAAI, pp. 226–231.

Fernández-Manso, A., Quintano, C., 2020. A synergetic approach to burned area mapping using maximum entropy modeling trained with hyperspectral data and VIIRS hotspots. Remote Sens. 12, 858. https://doi.org/10.3390/rs12050858.

Giglio, L., 2007. Characterization of the tropical diurnal fire cycle using VIRS and MODIS observations. Remote Sens. Environ. 108 (4), 407–421. https://doi.org/10.1016/j.rse.2006.11.018.

Giglio, L., Schroeder, W., 2014. A global feasibility assessment of the bi-spectral fire temperature and area retrieval using MODIS data. Remote Sens. Environ. 152, 166–173. https://doi.org/10.1016/j.rse.2014.06.010.

Giglio, L., Descloitres, J., Justice, C.O., Kaufman, Y.J., 2003. An enhanced contextual fire detection algorithm for MODIS. Remote Sens. Environ. 87 (2–3), 273–282. https://doi.org/10.1016/S0034-4257(03)00184-6.

Giglio, L., Randerson, J.T., Van Der Werf, G.R., 2013. Analysis of daily, monthly, and annual burned area using the fourth-generation global fire emissions database (GFED4). J. Geophys. Res. Biogeosci. 118 (1), 317–328. https://doi.org/10.1002/jgrg.20042.

Giglio, L., Schroeder, W., Justice, C.O., 2016. The collection 6 MODIS active fire detection algorithm and fire products. Remote Sens. Environ. 178, 31–41. https://doi.org/10.1016/j.rse.2016.02.054.

Gonzi, S., Palmer, P.I., Paugam, R., Wooster, M., Deeter, M.N., 2015. Quantifying pyroconvective injection heights using observations of fire energy: sensitivity of spaceborne observations of carbon monoxide. Atmos. Chem. Phys. 15 (8), 4339–4355. https://doi.org/10.5194/acp-15-4339-2015.

Grell, G.A., Freitas, S.R., 2014. A scale and aerosol aware stochastic convective parameterization for weather and air quality modeling. Atmos. Chem. Phys. 14 (10), 5233–5250. https://doi.org/10.5194/acp-14-5233-2014.

Gunapala, S.D., Johnson, W.R., Ting, D.Z., Soibel, A., Rafol, S.B., Keo, S.A., Pepper, B.J., Hill, C.J., Kalashnikova, O., Garay, M.J., Davies, A.G., Sood, A., Zeller, J., Lucey, P. G., Wright, R., Nunes, M., Babu, S., Ghuman, P., 2023a. Applications of T2SL barrier infrared detectors in observational instruments. In: Kimura, T., Babu, S.R., Hélière, A. (Eds.), Sensors, Systems, and Next-Generation Satellites XXVII. Presented at the Sensors, Systems, and Next-Generation Satellites XXVII, SPIE, Amsterdam, Netherlands, p. 25. https://doi.org/10.1117/12.2679191.

Gunapala, S.D., Ting, D., Johnson, W., Soibel, A., Ramsey, P., Kalashnikova, O., Garay, M., Davies, A., Maruyama, Y., Fisher, J., Sood, A., Zeller, J., David, C., Babu, S., Ghuman, P., 2023b. Towards compact fire infrared radiance spectral tracker (c-FIRST). In: He, S., Vivien, L. (Eds.), Smart Photonic and Optoelectronic Integrated Circuits 2023. Presented at the Smart Photonic and Optoelectronic Integrated Circuits 2023. SPIE, San Francisco, United States, p. 24. doi:10.1117/12.2659034.

Hodshire, A.L., Ramnarine, E., Akherati, A., Alvarado, M.L., Farmer, D.K., Jathar, S.H., et al., 2021. Dilution impacts on smoke aging: evidence in Biomass Burning Observation Project (BBOP) data. Atmos. Chem. Phys. 21 (9), 6839–6855. https://doi.org/10.5194/acp-21-6839-2021.

Hook, S.J., Myers, J.S., Thome, K.J., Fitzgerald, M., Kahle, A.B., Airborne Sensor Facility NASA Ames Research Center, Crawford, J.H., Warneke, C., Schwarz, J.P., 2021. MODIS/ASTER Airborne Simulator (MASTER) MASTER: FIREX-AQ Airborne Campaign, Western-Central USA, Summer 2019. https://doi.org/10.3334/ORNLDAAC/1941.

Ichoku, C., Ellison, L., 2014. Global top-down smoke-aerosol emissions estimation using satellite fire radiative power measurements. Atmos. Chem. Phys. 14 (13), 6643–6667. https://doi.org/10.5194/acp-14-6643-2014.

Ichoku, C., Kaufman, Y.J., 2005. A method to derive smoke emission rates from MODIS fire radiative energy measurements. IEEE Trans. Geosci. Remote Sens. 43 (11), 2636–2649. https://doi.org/10.1109/TGRS.2005.857328.

Jaffe, D.A., O'Neill, S.M., Larkin, N.K., Holder, A.L., Peterson, D.L., Halofsky, J.E., Rappold, A.G., 2020. Wildfire and prescribed burning impacts on air quality in the United States. J. Air Waste Manage. Assoc. 70 (6), 583–615. https://doi.org/10.1080/10962247.2020.1749731.

Jin, X., Zhu, Q., Cohen, R.C., 2021. Direct estimates of biomass burning NO_x emissions and lifetimes using daily observations from TROPOMI. Atmos. Chem. Phys. 21 (20), 15569–15587. https://doi.org/10.5194/acp-21-15569-2021.

Johnson, M.S., Strawbridge, K., Knowland, K.E., Keller, C., Travis, M., 2021. Long-range transport of Siberian biomass burning emissions to North America during FIREX-AQ. Atmos. Environ. 252, 118241. https://doi.org/10.1016/j.atmosenv.2021.118241.

Juang, C.S., Williams, A.P., Abatzoglou, J.T., Balch, J.K., Hurteau, M.D., Moritz, M.A., 2022. Rapid growth of large forest fires drives the exponential response of annual forest-fire area to aridity in the Western United States. Geophys. Res. Lett. 49 (5), e2021GL097131. https://doi.org/10.1029/2021GL097131.

Kahn, R.A., Li, W.-H., Moroney, C., Diner, D.J., Martonchik, J.V., Fishbein, E., 2007. Aerosol source plume physical characteristics from space-based multiangle imaging. J. Geophys. Res. Atmos. 112 (D11), 2006JD007647. https://doi.org/10.1029/2006JD007647.

Kaiser, J.W., Heil, A., Andreae, M.O., Benedetti, A., Chubarova, N., Jones, L., et al., 2012. Biomass burning emissions estimated with a global fire assimilation system based on observed fire radiative power. Biogeosciences 9 (1), 527–554. https://doi.org/10.5194/bg-9-527-2012.

Kaufman, Y.J., Justice, C.O., Flynn, L.P., Kendall, J.D., Prins, E.M., Giglio, L., et al., 1998. Potential global fire monitoring from EOS-MODIS. J. Geophys. Res. Atmos. 103 (D24), 32215–32238. https://doi.org/10.1029/98JD01644.

Khan, K., Rehman, S.U., Asghar, S., Fong, S., Sarasvady, S., 2014. DBSCAN: Past, present and future. In: The Fifth International Conference on the Applications of Digital Information and Web Technologies (ICADIWT 2014). Presented at the 2014 Fifth International Conference on the Applications of Digital Information and Web Technologies (ICADIWT). IEEE, Bangalore, India, pp. 232–238. https://doi.org/10.1109/ICADIWT.2014.6814687.

Krawchuk, M.A., Moritz, M.A., 2011. Constraints on global fire activity vary across a resource gradient. Ecology 92 (1), 121–132. https://doi.org/10.1890/09-1843.1.

Lamsal, L.N., Duncan, B.N., Yoshida, Y., Krotkov, N.A., Pickering, K.E., Streets, D.G., Lu, Z., 2015. U.S. NO2 trends (2005–2013): EPA Air Quality System (AQS) data versus improved observations from the Ozone Monitoring Instrument (OMI). Atmos. Environ. 110, 130–143. https://doi.org/10.1016/j.atmosenv.2015.03.055.

Li, F., Zhang, X., Kondragunta, S., Csiszar, I., 2018. Comparison of fire radiative power estimates from VIIRS and MODIS observations. JGR-Atmos. 123, 4545–4563. https://doi.org/10.1029/2017JD027823.

Li, F., Zhang, X., Roy, D.P., Kondragunta, S., 2019. Estimation of biomass-burning emissions by fusing the fire radiative power retrievals from polar-orbiting and geostationary satellites across the conterminous United States. Atmos. Environ. 211, 274–287. https://doi.org/10.1016/j.atmosenv.2019.05.017.

Massman, W.J., 2012. Modeling soil heating and moisture transport under extreme conditions: forest fires and slash pile burns. Water Resour. Res. 48 (10), 2011WR011710. https://doi.org/10.1029/2011WR011710.

Mota, B., Wooster, M.J., 2018. A new top-down approach for directly estimating biomass burning emissions and fuel consumption rates and totals from geostationary satellite fire radiative power (FRP). Remote Sens. Environ. 206, 45–62. https://doi.org/10.1016/j.rse.2017.12.016.

Ouattara, B., Thiel, M., Sponholz, B., Paeth, H., Yebra, M., Mouillot, F., Kacic, P., Hackman, K., 2024. Enhancing burned area monitoring with VIIRS dataset: a case study in Sub-Saharan Africa. Sci. Remote Sens. 10, 100165. https://doi.org/10.1016/j.srs.2024.100165.

Pan, X., Ichoku, C., Chin, M., Bian, H., Darmenov, A., Colarco, P., Ellison, L., Kucsera, T., Da Silva, A., Wang, J., Oda, T., Cui, G., 2020. Six global biomass burning emission datasets: intercomparison and application in one global aerosol model. Atmos. Chem. Phys. 20, 969–994. https://doi.org/10.5194/acp-20-969-2020.

Peterson, D., Wang, J., 2013. A sub-pixel-based calculation of fire radiative power from MODIS observations: 2. Sensitivity analysis and potential fire weather application. Remote Sens. Environ. 129, 231–249. https://doi.org/10.1016/j.rse.2012.10.020.

Peterson, D., Wang, J., Ichoku, C., Hyer, E., Ambrosia, V., 2013. A sub-pixel-based calculation of fire radiative power from MODIS observations: 1. Remote Sens. Environ. 129, 262–279. https://doi.org/10.1016/j.rse.2012.10.036.

Peterson, D., Hyer, E., Wang, J., 2014. Quantifying the potential for high-altitude smoke injection in the North American boreal forest using the standard MODIS fire products and subpixel-based methods: Smoke Plume Height and MODIS Fire Data. J. Geophys. Res. Atmos. 119 (6), 3401–3419. https://doi.org/10.1002/2013JD021067.

Peterson, D.A., Thapa, L.H., Saide, P.E., Soja, A.J., Gargulinski, E.M., Hyer, E.J., et al., 2022. Measurements from inside a Thunderstorm Driven by Wildfire: The 2019 FIREX-AQ Field Experiment. Bull. Am. Meteorol. Soc. 103 (9), E2140–E2167. https://doi.org/10.1175/BAMS-D-21-0049.1.

Prins, E.M., Menzel, W.P., 1992. Geostationary satellite detection of bio mass burning in South America. Int. J. Remote Sens. 13 (15), 2783–2799. https://doi.org/10.1080/01431169208904081.

Prins, Elaine M., Feltz, J.M., Menzel, W.P., Ward, D.E., 1998. An overview of GOES-8 diurnal fire and smoke results for SCAR-B and 1995 fire season in South America. J. Geophys. Res. Atmos. 103 (D24), 31821–31835. https://doi.org/10.1029/98JD01720.

Reid, J.S., Hyer, E.J., Prins, E.M., Westphal, D.L., Zhang, J., Wang, J., et al., 2009. Global monitoring and forecasting of biomass-burning smoke: description of and lessons from the fire locating and modeling of burning emissions (FLAMBE) program. IEEE J. Sel. Top. Appl. Earth Obs. Remote Sens. 2 (3), 144–162. https://doi.org/10.1109/JSTARS.2009.2027443.

Rein, G., 2013. Smouldering fires and natural fuels. In: Belcher, C.M. (Ed.), Fire Phenomena and the Earth System, 1st ed. Wiley, pp. 15–33. https://doi.org/10.1002/9781118529539.ch2.

Rooney, B., Wang, Y., Jiang, J.H., Zhao, B., Zeng, Z.-C., Seinfeld, J.H., 2020. Air quality impact of the Northern California Camp Fire of November 2018. Atmos. Chem. Phys. 20 (23), 14597–14616. https://doi.org/10.5194/acp-20-14597-2020.

Schmidt, C., 2020. Monitoring fires with the GOES-R series. In: The GOES-R Series. Elsevier, pp. 145–163. https://doi.org/10.1016/B978-0-12-814327-8.00013-5.

Schmidt, C.C., Prins, E.M., 2003, November. GOES wildfire ABBA applications in the western hemisphere. In: 2nd International Wildland Fire Ecology and Fire Management Congress and 5th Symp. on Fire and Forest Meteorology. Citeseer.

Schmit, T.J., Griffith, P., Gunshor, M.M., Daniels, J.M., Goodman, S.J., Lebair, W.J., 2017. A closer look at the ABI on the GOES-R series. Bull. Am. Meteorol. Soc. 98, 681–698. https://doi.org/10.1175/BAMS-D-15-00230.1.

Schroeder, W., Prins, E., Giglio, L., Csiszar, I., Schmidt, C., Morisette, J., Morton, D., 2008. Validation of GOES and MODIS active fire detection products using ASTER and ETM+ data. Remote Sens. Environ. 112 (5), 2711–2726. https://doi.org/10.1016/j.rse.2008.01.005.

Schroeder, W., Csiszar, I., Giglio, L., Schmidt, C.C., 2010. On the use of fire radiative power, area, and temperature estimates to characterize biomass burning via moderate to coarse spatial resolution remote sensing data in the Brazilian Amazon. J. Geophys. Res. Atmos. 115 (D21), 2009JD013769. https://doi.org/10.1029/2009JD013769.

Schroeder, W., Oliva, P., Giglio, L., Csiszar, I.A., 2014. The New VIIRS 375 m active fire detection data product: algorithm description and initial assessment. Remote Sens. Environ. 143, 85–96. https://doi.org/10.1016/j.rse.2013.12.008.

Schueler, C.F., Clement, J.E., Ardanuy, P.E., Welsch, C., DeLuccia, F., Swenson, H., 2002. NPOESS VIIRS sensor design overview. In: Barnes, W.L. (Ed.), Presented at the International Symposium on Optical Science and Technology, San Diego, CA, pp. 11–23. https://doi.org/10.1117/12.453451.

Seiler, W., Crutzen, P.J., 1980. Estimates of gross and net fluxes of carbon between the biosphere and the atmosphere from biomass burning. Clim. Chang. 2 (3), 207–247. https://doi.org/10.1007/BF00137988.

Shi, H., Jiang, Z., Zhao, B., Li, Z., Chen, Y., Gu, Y., et al., 2019. Modeling study of the air quality impact of record-breaking Southern California Wildfires in December 2017. J. Geophys. Res. Atmos. 124 (12), 6554–6570. https://doi.org/10.1029/2019JD030472.

Shivanasab, P., Abbaspour, R.A., Chehreghan, A., 2021. An assessment on the performance of the shape functions in clustering based on representative trajectories of dense areas. GISci. Remote Sens. 58, 1219–1249. https://doi.org/10.1080/15481603.2021.1973217.

Sofan, P., Bruce, D., Jones, E., Marsden, J., 2019. Detection and validation of tropical peatland flaming and smouldering using Landsat-8 SWIR and TIRS bands. Remote Sens. 11 (4), 465. https://doi.org/10.3390/rs11040465.

Thapa, L.H., Ye, X., Hair, J.W., Fenn, M.A., Shingler, T., Kondragunta, S., et al., 2022. Heat flux assumptions contribute to overestimation of wildfire smoke injection into the free troposphere. Commun. Earth Environ. 3 (1), 236. https://doi.org/10.1038/s43247-022-00563-x.

Toon, O.B., Maring, H., Dibb, J., Ferrare, R., Jacob, D.J., Jensen, E.J., et al., 2016. Planning, implementation, and scientific goals of the studies of emissions and atmospheric composition, clouds and climate coupling by regional surveys (SEAC [4] RS) field mission. J. Geophys. Res. Atmos. 121 (9), 4967–5009. https://doi.org/10.1002/2015JD024297.

Val Martin, M., Heald, C.L., Lamarque, J.-F., Tilmes, S., Emmons, L.K., Schichtel, B.A., 2015. How emissions, climate, and land use change will impact mid-century air quality over the United States: a focus on effects at national parks. Atmos. Chem. Phys. 15 (5), 2805–2823. https://doi.org/10.5194/acp-15-2805-2015.

Van Der Werf, G.R., Randerson, J.T., Giglio, L., Van Leeuwen, T.T., Chen, Y., Rogers, B. M., et al., 2017. Global fire emissions estimates during 1997–2016. Earth Syst. Sci. Data 9 (2), 697–720. https://doi.org/10.5194/essd-9-697-2017.

Warneke, C., Schwarz, J.P., Dibb, J., Kalashnikova, O., Frost, G., Al-Saad, J., et al., 2023. Fire influence on regional to global environments and air quality (FIREX-AQ). J. Geophys. Res. Atmos. 128 (2), e2022JD037758. https://doi.org/10.1029/2022JD037758.

Westerling, A.L., 2016. Correction to 'Increasing western US forest wildfire activity: sensitivity to changes in the timing of spring'. Phil. Trans. Roy. Soc. B Biol. Sci. 371 (1707), 20160373. https://doi.org/10.1098/rstb.2016.0373.

Whitburn, S., Van Damme, M., Kaiser, J.W., Van Der Werf, G.R., Turquety, S., Hurtmans, D., et al., 2015. Ammonia emissions in tropical biomass burning regions: Comparison between satellite-derived emissions and bottom-up fire inventories. Atmos. Environ. 121, 42–54. https://doi.org/10.1016/j.atmosenv.2015.03.015.

Wiedinmyer, C., Akagi, S.K., Yokelson, R.J., Emmons, L.K., Al-Saadi, J.A., Orlando, J.J., Soja, A.J., 2011. The Fire INventory from NCAR (FINN): a high resolution global model to estimate the emissions from open burning. Geosci. Model Dev. 4 (3), 625–641. https://doi.org/10.5194/gmd-4-625-2011.

Wiedinmyer, Christine, Kimura, Y., McDonald-Buller, E.C., Emmons, L.K., Buchholz, R. R., Tang, W., et al., 2023. The Fire Inventory from NCAR version 2.5: an updated global fire emissions model for climate and chemistry applications. Geosci. Model Dev. 16 (13), 3873–3891. https://doi.org/10.5194/gmd-16-3873-2023.

Wiggins, Elizabeth B., Soja, A.J., Gargulinski, E., Halliday, H.S., Pierce, R.B., Schmidt, C. C., et al., 2020. High temporal resolution satellite observations of fire radiative power reveal link between fire behavior and aerosol and gas emissions. Geophys. Res. Lett. 47 (23), e2020GL090707. https://doi.org/10.1029/2020GL090707.

Wiggins, E.B., Anderson, B.E., Brown, M.D., Campuzano-Jost, P., Chen, G., Crawford, J., et al., 2021. Reconciling assumptions in bottom-up and top-down approaches for estimating aerosol emission rates from wildland fires using observations from FIREX-AQ. J. Geophys. Res. Atmos. 126 (24), e2021JD035692. https://doi.org/10.1029/2021JD035692.

Wilmot, T.Y., Mallia, D.V., Hallar, A.G., Lin, J.C., 2022. Wildfire plumes in the Western US are reaching greater heights and injecting more aerosols aloft as wildfire activity intensifies. Sci. Rep. 12 (1), 12400. https://doi.org/10.1038/s41598-022-16607-3.

Wolfe, R.E., Lin, G., Nishihama, M., Tewari, K.P., Tilton, J.C., Isaacman, A.R., 2013. Suomi NPP VIIRS prelaunch and on-orbit geometric calibration and characterization. J. Geophys. Res. Atmos. 118 (20). https://doi.org/10.1002/jgrd.50873.

Wooster, M.J., Roberts, G., Perry, G.L.W., Kaufman, Y.J., 2005. Retrieval of biomass combustion rates and totals from fire radiative power observations: FRP derivation and calibration relationships between biomass consumption and fire radiative energy release. J. Geophys. Res. Atmos. 110 (D24), 2005JD006318. https://doi.org/10.1029/2005JD006318.

Wooster, M.J., Zhukov, B., Oertel, D., 2003. Fire radiative energy for quantitative study of biomass burning: derivation from the BIRD experimental satellite and comparison to MODIS fire products. Remote Sens. Environ. 86, 83–107. https://doi.org/10.1016/S0034-4257(03)00070-1.

Xiong, X., Butler, J., Chiang, K., Efremova, B., Fulbright, J., Lei, N., et al., 2014. VIIRS on-orbit calibration methodology and performance. J. Geophys. Res. Atmos. 119 (9), 5065–5078. https://doi.org/10.1002/2013JD020423.

Ye, X., Arab, P., Ahmadov, R., James, E., Grell, G.A., Pierce, B., et al., 2021. Evaluation and intercomparison of wildfire smoke forecasts from multiple modeling systems for the 2019 Williams Flats fire. Atmos. Chem. Phys. 21 (18), 14427–14469. https://doi.org/10.5194/acp-21-14427-2021.

Zhang, C., Heinson, W.R., Garay, M.J., Kalashnikova, O., Chakrabarty, R.K., 2021. Polarimetric sensitivity of light-absorbing carbonaceous aerosols over ocean: A theoretical assessment. J. Quant. Spectrosc. Radiat. Transf. 272, 107759. https://doi.org/10.1016/j.jqsrt.2021.107759.

Zhuang, Y., Fu, R., Santer, B.D., Dickinson, R.E., Hall, A., 2021. Quantifying contributions of natural variability and anthropogenic forcings on increased fire weather risk over the western United States. Proc. Natl. Acad. Sci. 118 (45), e2111875118. https://doi.org/10.1073/pnas.2111875118.